

Correlative elemental and electrical micro-analysis of laser fired
contacts in silicon solar cells
by

Patricia Yen

B.S. in Engineering Physics
B.A. in Luso-Brazilian Language and Literature
University of California, Berkeley, 2014

Submitted to the Department of Mechanical Engineering
in partial fulfillment of the requirements for the degree of
Master of Science in Mechanical Engineering

at the

MASSACHUSETTS INSTITUTE OF TECHNOLOGY

September 2016

© 2016 Massachusetts Institute of Technology. All rights reserved.

Author.....
Department of Mechanical Engineering
August 4, 2016

Certified by.....
Tonio Buonassisi
Associate Professor of Mechanical Engineering
Thesis Supervisor

Accepted by.....
Rohan Abeyaratne
Professor of Mechanical Engineering
Chairman, Department Committee on Graduate Theses

Correlative elemental and electrical micro-analysis of laser fired contacts in silicon solar cells

by

Patricia X. T. Yen

Submitted to the Department of Mechanical Engineering
on August 4, 2016 in Partial Fulfillment of the
Requirements for the Degree of Master of Science in
Mechanical Engineering

ABSTRACT

Photovoltaic (PV) energy is an abundant and clean alternative to conventional energy sources, which pose an irreversible threat to the environment. For PV to reach cost parity with conventional energy, advances like laser-fired contacts must be adopted to improve cost levers like solar cell efficiency and industrial throughput.

This work examines the relationship between laser-processing on the structure and property of solar cells, with the goal of (1) characterizing the differences between using two lasers simultaneously (double-shot lasing) versus a single laser for LFC processing, and (2) using the new findings to optimize industrial LFC efforts. Electrical properties such as lifetime degradation and contact resistance are evaluated using photoluminescence imaging and transmission line measurements, respectively. LFC structures are studied using scanning electron microscope and elemental mapping tools like micro-X-ray fluorescence microscopy and energy dispersive spectroscopy.

For the conditions studied, it is unclear whether double-shot lasing can produce higher-quality LFCs than single-shot lasing, although results suggest that the infrared laser influences electrical properties more than the green laser. For future LFC optimization, the μ -XRF maps of elemental distribution may offer a novel way to evaluate LFC formation.

Thesis Supervisor: Tonio Buonassisi
Title: Associate Professor of Mechanical Engineering

Thesis Supervisor: Ian Marius Peters
Title: Research Scientist

ACKNOWLEDGEMENTS

I would like to express a tremendous amount of gratitude to those who have been part of my graduate school journey. It has been a rewarding and challenging experience, and I could not have done it alone.

I would like to thank my family. I would not be where I am now without their love and support.

I would like to thank Prof. Buonassisi for his encouragement and time. It has been inspiring to work in the PV Lab and see the depth and range of impact one person can have.

I would like to thank the supportive and kind members of the MIT PV Lab for helping me learn and grow as a scientist. I would like to especially like to thank those who have been contributed to my thesis work: Ashley Morishige, who answered my questions with thoroughness and shared her expertise and support at the synchrotron; Mallory Jensen, for her support and mentorship that guided me along the project; Dr. Sergio Castellanos, for teaching me to conduct and interpret results from energy dispersive spectroscopy; Dr. Austin Akey for his guidance and expertise throughout the project; Dr. Tim Kirkpatrick for his mentorship; Dr. Maulid Kivambe for teaching me to conduct and interpret results from the scanning electron microscope; and Dr. Marius Peters for close reading of my thesis.

I also deeply appreciate the efforts of Dr. Steve Hegedus, Dr. Jianbo He, and Mr. Ujjwal Das for fabricating the samples for this study; Dr. Marco Mendes and Dr. Xiaoyong Song for laser processing the samples; and these five individuals for insightful discussions and experimental analysis. I also want to thank Dr. Barry Lai at Argonne National Laboratory for assistance in processing the μ -XRF data.

Last but not least, I am thankful to the many faces of MIT and Cambridge where I have found friendship, community, and help.

This research was made possible by funding from the National Science Foundation Graduate Research Fellowship Program and grants from the National Science Foundation and the U.S. Department of Energy.

ABBREVIATIONS

Abbreviation	Description
E_i	Initial energy level of an electron
E_h	Higher energy level of a n electron
E_g	Bandgap energy
SRV	Surface recombination velocity
J_0	dark saturation current density
J_L	photogenerated current
J	net current density
V	voltage applied acrossd diode
q	Charge of an electron
k	Boltzmann's constant
T	Absolute temperature
V_{oc}	Open-circuit voltage
$I-V$	Current-voltage
J_{sc}	Short-circuit current density
J_{mpp}	Current density at the maximum power point
V_{mpp}	Voltage at the maximum power point
FF	Fill factor
P_{in}	Total power density of incident radiation
Al-BSF	Aluminum back surface field
PERC	Passivate emitter and rear contact
IBC	Interdigitated back contact
LFC	Laser-fired contact
IR	infrared
SiN_x	Silicon nitride
PCD	Photoconductance decay
PC-PLI	Photoconductance-calibrated photoluminescence imaging
RF	Radio frequency
QSS	Quasi-steady-state
CCD	Charge-coupled device
τ_{eff}	Effective minority carrier lifetime
τ_{bulk}	Bulk minority carrier lifetime
τ_s	Surface minority carrier lifetime
W	Wafer thickness
S	Surface recombination velocity
D_n	Diffusivity constant
TLM	Transmission line measurement
R_C	Contact resistance
R_T	Total resistance
l	Distance between measured contacts in TLM
R_{SK}	Modified sheet resistance under contact
L_T	Transfer length

w	Width of contact
EDS	Energy dispersive spectroscopy
SEM	Scanning electron microscope
μ -XRF	Micro-x-ray fluorescence spectroscopy
a.u.	Arbitrary units
Si:Al	Ratio of silicon counts to aluminum counts

CONTENTS

Abstract	2
Acknowledgements.....	3
Abbreviations	4
Contents.....	6
Figures	8
Tables.....	10
1 Introduction.....	11
1.1 Motivation.....	11
1.1.1 Objectives.....	11
1.1.2 Basics of silicon solar cells	11
1.1.3 State of the art of PV contacts	16
1.1.4 Next generation cell architectures	18
1.2 Background of Laser-Fired Contacts	19
1.2.1 LFC lasing process.....	20
1.2.2 LFC state of the art.....	22
1.2.3 Previous LFC characterization efforts.....	23
1.3 Current challenges to implementing LFC's in the market	25
1.4 Approach.....	26
2 Methods	27
2.1 Sample preparation	27
2.2 LFC Lasing Parameters	29
2.3 Characterization Techniques	30
2.3.1 Electrical Characterization	30
2.3.1.1 Photoconductance-calibrated Photoluminescence Imaging (PC-PLI)	30
3. Experimental Results	31
3.1 PL Images	31
3.2 Transmission line measurements of specific contact resistance.....	33

3.3 μ-X-ray fluorescence spectroscopy for elemental mapping	34
3.4 SEM and EDS	36
4. Discussion	39
4.1 Expected property-process relationships of two-laser firing	39
4.2 Structure-property-process relationships.....	40
4.2.1 Property-process relationship: PLI measurements	40
4.2.3 Property-process relationship: TLM measurements.....	42
4.2.2 Structure-property-process relationship.....	43
4.3 XRF vs. EDS	49
5. Summary & Conclusion	51
Bibliography	53

FIGURES

Figure 1 The basic elements of a solar cell include contacts, an absorber, and a junction that separates charge carriers. Image modified from [11]	12
Figure 2 I-V curve for an illuminated cell.....	15
Figure 3 An image of the cross-section of the rear aluminum contact and the eutectic layers in an Al-BSF cell [10].....	17
Figure 4 A comparison of the LFC process and the localized contacting process for point contact patterning on passivated rear silicon solar cells [30].	19
Figure 5 A figure showing the bulk silicon, passivation layer, and aluminum layers in a laser-fired contact material stack. [48].....	20
Figure 6 A scanning electron micrograph (SEM) (left) and optical profilometry measurement (right) showing the characteristic inner crater and outer aluminum ring for an LFC fired with a microsecond pulse. [69]	23
Figure 7 The material stack of the samples used to test different LFC lasing parameters. The layers are not to scale.	28
Figure 8 A diagram showing the rear of the sample. Individual LFC spots were fired into the metallized strips. Each row corresponds to a new lasing condition. The dimensions are not to scale.	29
Figure 9 PL images of one sample taken (a) before laser processing, (b) after lasing processing with sampled linescans shown in color, and the corresponding plot of PL intensity shown for the linescans.	32
Figure 10 A row of LFC strips that is used for TLM measurements. One data set corresponds to the resistance measurements between one strip and every other strip.....	33
Figure 11 The material stack of the samples used to test different LFC lasing parameters, with the incident laser and lased region shown. The layers are not to scale and the thicknesses are listed in 2.1 Sample preparation(pg. 26).....	39
Figure 12 A plot of PLI contrast values versus the green laser energy dose, showing that PLI contrast primarily depends on the IR laser.....	41

Figure 13 The R_C data from Table 3 plotted against green energy dose. Group 2 corresponds to the red symbols, and Group 3 corresponds to the blue symbols. Group 1 is not shown because contact was not measured.....	43
Figure 14 (a) EDS maps, (b) μ -XRF maps, and (c) two SEM images of the same “IR 2” spot, which highlight different features. The scale bar shown applies to all maps. The same μ -XRF maps were shown in Table 4 (34), but in \log_{10} scale. Here, the maps are linear.....	49

TABLES

Table 1 A summary of the four lasing parameters used to fire LFCs in this study.	29
Table 2 Contrast values for different lasing conditions.....	33
Table 3 R_c for different lasing conditions as measured by TLM.	34
Table 4 μ -XRF maps showing counts for silicon, aluminum, antimony, titanium, and Si:Al.....	35
Table 5 The Si:Al values for each of the lasing conditions.....	36
Table 6 SEM images showing contacts that were fired with each lasing condition.	37
Table 7 SEM images of larger LFC and smaller LFCs.....	42
Table 8 The tested lasing conditions are categorized into Group 1, Group 2, and Group 3	44
Table 9 Data for Group 1, along with SEM images and XRF maps	45
Table 11 Selected SEM micrographs and data of Group 1 conditions.	47
Table 12 A summary of data, XRF maps, and SEM images for Group 3.....	48

1 Introduction

1.1 Motivation

1.1.1 Objectives

Anthropogenic carbon dioxide emissions pose an urgent threat to the environment and global human development [1], [2]. Conventional power plants are the largest source of U.S. emissions, accounting for 40% of American greenhouse gas pollution [3]. While solar energy is an abundant and clean alternative, the cost of photovoltaic (PV) manufacturing remains a significant barrier to its widespread deployment [4]. For utility-scale and subsidy-free adoption, manufacturing costs for the standard silicon PV modules must drop to \$.75/W to reach cost parity with conventional energy sources [4], [5]. This translates into a need for cheaper, scalable processes that can simultaneously push PV technology past the current industry average of 16% cell efficiency [6].

Since their invention in the 1950s, silicon solar cells have dominated the photovoltaic market [7]. To extract charge, metal contacts are typically applied to silicon solar cells using a relatively simple screen-printing process [8]. Because cost is strongly correlated with cell efficiency, higher-efficiency PV device architectures have emerged. These require local contacts, which involve local alloying of metals through a passivation layer [9]. The foundational study of laser-metal-dielectric-silicon interactions becomes important for understanding and optimizing local contact formation.

1.1.2 Basics of silicon solar cells

In a solar cell, incident light produces a voltage difference at the junction of two different materials. This effect is called the photovoltaic effect, which makes a solar cell work. A solar cell consists of at least three basic elements: an absorber, a junction, and contacts. The photovoltaic effect can be considered as three basic processes, which take place in the solar cell:

- 1) An absorber (typically silicon) absorbs incoming photons, and charge carriers are generated
- 2) A junction facilitates charge carrier separation
- 3) Contacts at the junction terminals collect carriers and pass them through to an external load [10]

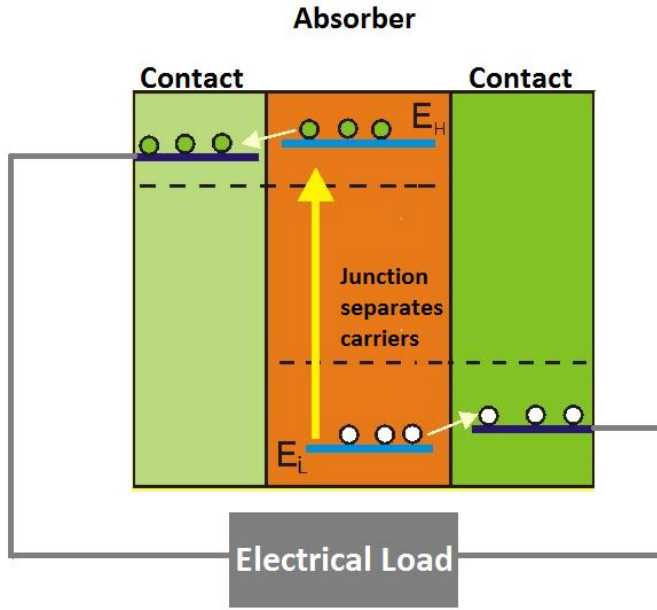


Figure 1 The basic elements of a solar cell include contacts, an absorber, and a junction that separates charge carriers. Image modified from [11]

When a photon is absorbed by a material, the photon's energy excites an electron from an initial energy level (E_i) to a higher energy level (E_h). Photons can be absorbed and generate an electron-hole pair if the photon energy exceeds the bandgap energy (E_g). This process is shown for an ideal semiconductor in Figure 1. The excitation of the electron to the higher energy level results in a hole, which behaves like a positively charged particle. Consequently, the absorption of one photon results in an electron-hole pair.

The electron-hole pair can recombine, meaning that the electron can relax back to the valence band and eliminate the hole. This is a non-ideal process that limits the separation and collection of free carriers. This can happen through radiative recombination, when the energy is released as a photon, or non-radiative recombination, when the energy is transferred to other charge carriers or lattice vibrations. To prevent recombination, the absorber should have selective interfaces on both sides that allow only one type charge carrier to flow out of each. This means that electrons can only exit the absorber on one side, and holes can only exit the absorber on the other side. Silicon solar cells use *n*- and *p*-type material as the selective interfaces.

There are three recombination mechanisms, which can occur in parallel.

- 1) Radiative recombination is the reverse process of absorption. An electron that is in a higher non-equilibrium energy state emits a photon and relaxes back to an empty lower-energy state. The energy of the photon is equal to the difference in energy states.
- 2) Auger recombination involves an electron recombining with a hole and emitting extra energy to another electron, rather than a photon.
- 3) Shockley-Read-Hall recombination involves elemental impurities and structural defects that introduce energy levels into the band gap. These defect levels create a two-step recombination process, in which electrons relax from the conduction band energy state to the defect level, then combine with a hole in the valence band. In the case of thermally oxidized silicon, the surface recombination velocity is in the range of 1-10 cm/s for doping impurities $<10^{17} \text{ cm}^{-3}$ [12]. For larger concentrations, the SRV increases rapidly [13].

Recombination occurs in the bulk and surface of a semiconductor. The bulk refers to material characterized by uniform properties, as measured in sections that are sufficiently far from a sample's boundaries [14]. The surfaces of semiconductors are sites of severe defects in the crystal structure and introduce a large density of defect states within the bandgap. In a silicon wafer, surface interfaces arise when silicon abruptly encounters either a metallized or non-metallized surface. Metal-silicon interfaces can result in more than 50% of losses due to recombination in high-efficiency cells and exhibit very high surface recombination velocities (SRVs), which define the rate of recombination at surfaces [6], [15]. In semiconductor heterostructures, interface recombination occurs by the same mechanism [16]. At interfaces, SRV can significantly reduce solar cell efficiency and is mainly affected by the density and character of interface states [17].

SRV is largely influenced by the density and types of defect states that are introduced by dangling silicon bonds at the surface. To reduce these defect states, a process called "passivation" is used to protect the surface of a semiconductor. Chemical passivation creates a layer of material that saturates the dangling bonds at the surface [16]. Passivation layers at interfaces are ideal because they can minimize carrier recombination and improve minority carrier lifetimes. There are two ways to passivate silicon. One way is by chemical passivation of the surface, while the other way involves the field effect.

In field-effect passivation, a potential barrier can prevent minority carriers from reaching the surface [18]. The standard passivation method is thermal oxidation at a high temperatures to

grow a dielectric film. During the oxidation process, the interface between the oxide and silicon moves into the relatively defect-free bulk, reducing the density of interface states [17].

Chemical passivation involves the immersion of silicon wafers into liquids that can saturate the dangling silicon surface bonds. This occurs by using thin chemical oxide layers or hydrogen-termination to cover the surface [19]. In hydrogen-termination, the native silicon diode is first etched off the silicon surface using a hydrogen fluoride solution. The resulting surface silicon atoms are covalently bonded to hydrogen [20]–[22]. This passivation method does not persist and can only saturate the surface bonds for a short period of time [23].

When the diode is illuminated, the photovoltaic effect drives current through the device [24]. Photogenerated carriers result in a current as electrons move to the *n*-type side and holes to the *p*-type side of the junction. Under short-circuit conditions, charge does not build up and carriers exit the device as photogenerated current.

The current-voltage characteristics of a *pn*-junction can be approximated using the one-diode equation:

$$J = J_L - J_0 \left(e^{\frac{qV}{nKT}} - 1 \right) \quad \text{Eq. 1}$$

Here, J_0 represents the dark saturation current density, or the diode leakage current density when unilluminated, J is the net current density that flows through the diode, J_L is the photogenerated current, V is voltage applied across the diode, q is the charge of an electron, k is Boltzmann's constant, and T is the absolute temperature [25].

Under illumination, photogenerated carriers build up as electrons on the *n*-type side and holes on the *p*-type side. This charge separation creates an electric field that opposes the existing electric field in the junction, which reduces the net field and allows current to flow.

Under open-circuit conditions, the forward bias of the junction increases to a point where resulting net current is zero. The voltage needed to balance these currents is called the “open-circuit voltage,” or V_{oc} .

The external electrical characteristics of a solar cell are determined by illuminating the solar cell under standard testing conditions and measuring the current while biasing the cell at the

terminals. An example of the resulting *I-V* curve can be seen in Figure 2 *I-V* curve for an illuminated cell.

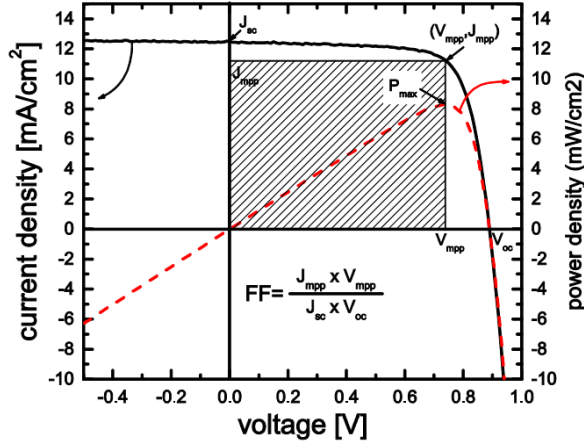


Figure 2 *I-V* curve for an illuminated cell

The primary *I-V* parameters are:

- J_{SC} , or the short-circuit current density, which is the current generated at zero voltage. J_{SC} is determined by optical and recombination losses.
- V_{OC} , or the open-circuit voltage, is the voltage generated at zero current. V_{OC} is the maximum voltage available from a solar cell and corresponds to the amount of bias on the cell. V_{OC} occurs at short-circuit current conditions and can be found by setting the net current equal to zero in the one diode equation:

$$V_{OC} = \frac{n k T}{q} \ln \left(\frac{J_L}{J_0} + 1 \right) \quad \text{Eq. 2}$$

V_{OC} is determined by the material bandgap, carrier recombination, and temperature

- J_{mpp} and V_{mpp} , the current density and voltage at the maximum power point (mpp) of the *I-V* curve
- FF , or the fill factor, which refers to the largest rectangle that will fit in the *I-V* curve of a diode.
- The power conversion efficiency of the solar cell, which can be calculated as

$$\eta = \frac{P_{\max}}{P_{\text{in}}} = \frac{V_{\text{OC}} J_{\text{SC}} FF}{P_{\text{in}}} = \frac{V_{\text{mpp}} J_{\text{mpp}}}{P_{\text{in}}} \quad \text{Eq. 3}$$

where P_{in} is the total power density of the incident radiation. Under standard testing conditions, P_{in} is taken to be 1000 W/m².

The maximum power output of a solar cell is defined by V_{OC} , J_{SC} , and FF . Since J_{SC} is already near its maximum, V_{OC} can only be increased by decreasing J_0 . J_0 is directly related to recombination, which was described earlier in this section. From Eq. 2 and Eq. 3, it is clear that increased recombination limits V_{OC} and power conversion efficiency [26].

1.1.3 State of the art of PV contacts

Since their invention in the 1950's, crystalline silicon solar cells have dominated over 80% of the PV market [27]. In industry today, the standard architecture for a silicon solar cell is the co-fired, screen-printed aluminum back surface field (Al-BSF) cell. The top layer on the front of an Al-BSF cell is doped to form a *pn*-junction and to allow electrical conduction to efficiently transport majority carriers to the contacts. A passivation layer is grown on top of the silicon, then metal contacts are screen-printed on so the silver paste punctures the passivation layer and contacts the silicon. An array of busbars and contact fingers are soldered on for carrier transport [28].

The rear side of an Al-BSF cell is fully metallized for efficient carrier transport. A small percent of the area is used for contact pads that are screen-printed as in the front contacts. The remaining area mixes with the underlying silicon to form a homogeneous mixture, or a eutectic, which provides low contact resistance and a passivating back-surface field. Because of its long-standing use, screen-printing electrical contacts is advantageous because equipment is widely available and continually improving. Compared to new contacting methods, screen-printing offers lower risk and capital investment for new manufacturing operations, as experience and equipment are both accessible.

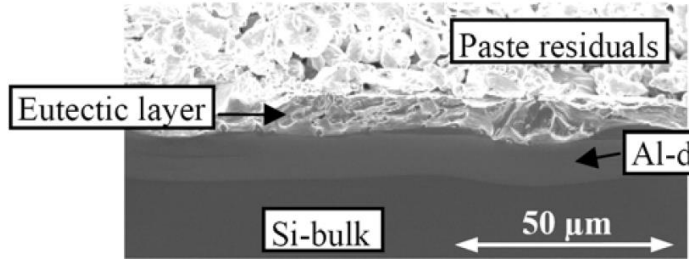


Figure 3 An image of the cross-section of the rear aluminum contact and the eutectic layers in an Al-BSF cell [10]

Despite the simplicity and popularity of screen-printing, it presents limitations that impede the cost reduction of photovoltaics. The commercial success of photovoltaics is contingent upon cost, which can be targeted using three levers: material cost, efficiency, and manufacturing cost [27]. One major disadvantage to screen-printing is wafer warping, which imposes a bottom limit on the first cost lever, material cost [29]. After a silicon wafer is screen-printed with a metal paste, it is fired at a high temperature and cooled to form a eutectic and the BSF, as seen in Figure 3. The silicon cools and recrystallizes to form a BSF that enables low recombination around the contacts [30]–[32]. During this cooling process, the silicon warps significantly, inducing low mechanical yield that worsens significantly with thin wafers.

As wafer thickness approaches 100-200 μm to reduce materials cost, screen-printing will require a trade-off between thickness and yield that restricts the ability to lower costs [33]. Over the last decade, absolute wafer thickness has been a consistent cost-reduction measure and has dropped by about 100 μm in the last decade [33]. This is expected to further decrease, as advances in automation and cell processing enable more effective handling of thin wafers.

Another drawback to screen-printing is that commercial cells that contacts are limited to efficiencies of 19%, with modules limited to efficiencies of 15% [34]. This places another limit on how much costs can be lowered due to efficiency. In comparison, industrial targets are between 25-30%, approaching the theoretical efficiencies for single-junction silicon solar cells [35]. Significant research efforts focus cost levers that can make solar energy cost competitive with conventional energy sources.

1.1.4 Next generation cell architectures

Advanced cell architectures that use novel contacting techniques have the potential to lower the cost of PV by improving both device and manufacturing efficiencies. One promising new architecture is the Passivated Emitter and Rear Contact (PERC) solar cell. This architecture proposes that a dielectric layer is deposited onto the rear, then point electrical contacts can be made to the bulk material. The passivation layer results in a lower surface recombination velocity and prevents wafer warping. Furthermore, the dielectric layer can serve as an optical back-surface mirror, possibly improving light trapping abilities that are critical for high efficiencies on the thin substrates that are used for PERC and other advanced architectures that minimize material costs [10], [28], [31], [36]. PERC cells are expected to enable conversion efficiencies of 25% on the commercial scale [37].

Another promising architecture is Sunpower's interdigitated back contact (IBC) solar cell, which places all contacts on the rear to maximize the front surface area available for light absorption. The resulting back contacts alternate between p^+ and n^+ fingers, requiring multiple localized junctions instead of a single large pn -junction. The semiconductor-metal interfaces must also be minimized to reduce recombination at defect-rich interfaces. Heterojunction silicon architectures are especially promising because production efficiencies have already reached 22%, while IBC simulations predict 26% [38]. Laser-firing IBCs provides a method for low-cost, scalable manufacturing of high-efficiency PV cells [10], [28], [36], [38]–[40].

The IBC cell is considered to have the highest efficiency potential for conventional silicon solar cells [41]. By comparison, the typical Al-BSF cells that are produced from single crystal silicon and multi-crystalline silicon have efficiencies around 16% [42]. These advanced architectures, however, require a new contacting method that permits the local formation of aluminum silicide through a passivated silicon wafer. This contrasts with the Al-BSF contacting method, which uses screen-printed aluminum directly on top of the bulk material to form a large pn -junction on the rear.

To form the small, localized junctions necessary for PERC and IBC cells, conventional fabrication methods use photolithography and multiple handling steps that impede low-cost, large-scale manufacturing [31], [43], [44]. Such complexity thus prevents the widespread adoption of high-efficiency architectures that can help lower the cost of solar energy.

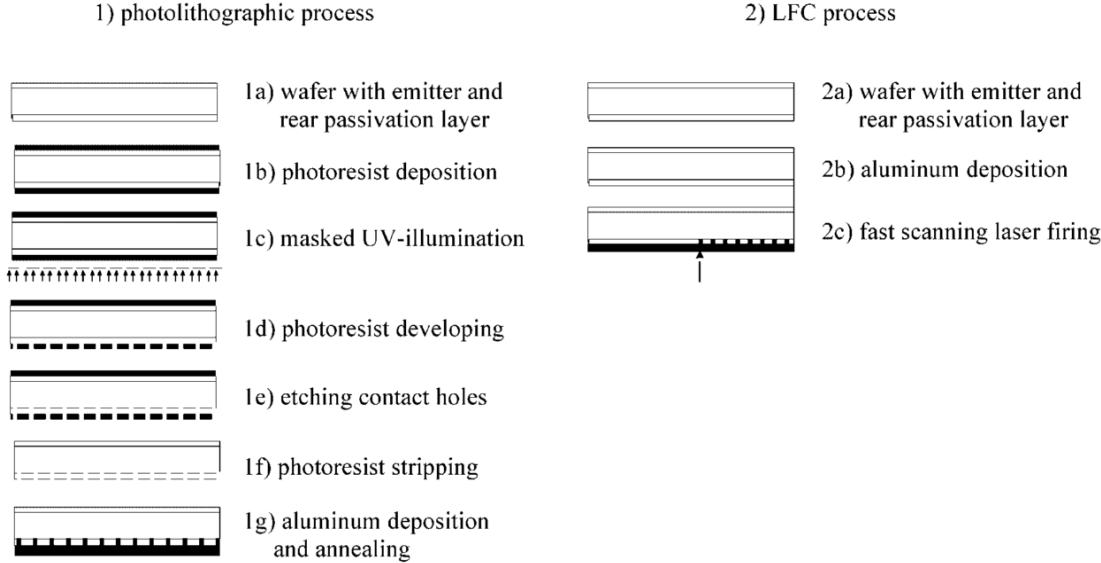


Figure 4 A comparison of the LFC process and the localized contacting process for point contact patterning on passivated rear silicon solar cells [30].

A simple, industrially-feasible way to achieve a passivated rear emerged with the development of the laser-fired contact (LFC). Before the LFC, manufacturers had already been able to successfully produce the thin wafers in architectures like PERC, and surface passivation was a well-understood, in-line process. Researchers thus turned their attention to lasers to form the ohmic point contacts in a scalable, low-cost way. As seen in Figure 4, the LFC process first involves the deposition of a dielectric passivation layer, then a metal layer on the rear of the solar cell. A laser then locally fires the pre-deposited metal through the dielectric layer, alloying the metal contact to the base to form a beneficial doped region [30], [45], [46].

1.2 Background of Laser-Fired Contacts

LFCs are an effective and industrially-feasible way to develop rear point contacts on silicon solar cells with passivated back surfaces. An LFC is formed by laser-firing a metal-dielectric-semiconductor stack. In silicon LFC cells, a ~50-100 nm dielectric such as silicon dioxide or silicon nitride is deposited on top of a ~250-300 μm bulk silicon for passivation and absorption [15]. Depending on the thickness of the dielectric, the material can act as an optical back-surface mirror that generates high internal back reflectance by returning unabsorbed photons back through the silicon to generate more charge carriers [9], [44]. A thicker metal layer, typically 2 μm aluminum, forms the rear surface of the solar cell. A laser locally fires the aluminum through the

dielectric layer. The molten aluminum alloys with the silicon bulk to form a point contact, while the local dielectric ablation limits the amount of bulk that is exposed and affected by surface recombination [45], [30], [47]. The ideal final product is shown in Figure 5.

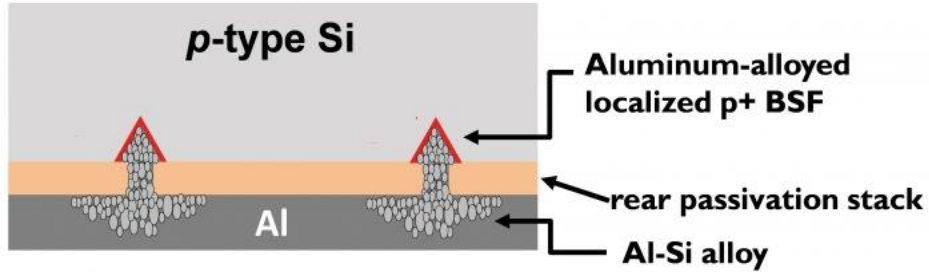


Figure 5 A figure showing the bulk silicon, passivation layer, and aluminum layers in a laser-fired contact material stack. [48]

Although *p*-type silicon is the dominant starting material for silicon solar cells, researchers have increasingly explored LFCs on *n*-type silicon as well. This is because the material properties of *n*-type silicon make it better suited to the cost-effective fabrication of high efficiency cells [49], [50]. In industry, *p*-type silicon has been favored because the formation an *n*-type emitter with phosphorous diffusion is relatively simple and doubles as a gettering process that improves material performance by reducing impurity concentrations [12], [51], [52]. In contrast, the formation of a *p*-type emitter on an *n*-type substrate requires a high-temperature boron diffusion process that is not optimal for industrial-scale production. LFCs can form local aluminum junctions that serve as *p*-type emitters, which has led to renewed interest in *n*-type silicon cells with LFCs [29].

1.2.1 LFC lasing process

The use of lasers in solar cell manufacturing has the potential to significantly improve fabrication throughput and cell efficiency, which are two essential factors in reducing the cost of PV [28]. Already, lasers have been used in industry for edge isolation, surface texturing, selective emitter doping, and wafer dicing [31], [53]–[56]. In comparison with the 13-step photolithography technique shown in Figure 4, laser firing reduces local rear contact formation to two deposition steps for the dielectric and metal stack, then the firing step. This streamlined process holds great

promise for the use of local rear contacts in high-efficiency architectures and their industrial success.

In the LFC process, a single laser is used in three stages:

1) Metal melting: the laser selectively heats and melts a spot on the rear aluminum contact layer. The metal melts and the local heat induces thermal and mechanical stress.

2) Dielectric ablation: The stress from the local heat ablates the passivation layer, leaving a hole that exposes the underlying silicon. As the laser heats the exposed silicon, it melts and is thermally expelled out of the hole [10], [53], [57], [58].

3) Metal-silicon alloying and contact formation: The high temperature reached in silicon in contact with aluminum increases the solubility and diffusivity of aluminum in silicon [43]. This facilitates the formation of the silicon-aluminum eutectic upon cooling, which provides an electrically conductive path out of the bulk [10], [32], [59].

The most commonly studied LFC process uses a single laser with 1064 nm wavelength to fire the material stack. Multiple parameters have been tested, including laser defocusing, the number of pulses per contact, and frequencies between 100 Hz and 30 kHz. [31], [32], [44], [57], [60]–[62]).

Damage is the primary concern with the LFC process. The laser process introduces a large amount of energy to a small volume (the affected surface area is on the order of $50 \mu\text{m}^2$), which results in significant structural damage to the substrate and passivation surrounding the contact. An excess of laser energy can cause defects in the silicon crystalline structure. These defects can act as recombination centers, reducing the number of carriers available for collection and device performance. In processes that use an aluminum contact layer, LFCs incorporate a localized BSF due to the final aluminum-silicon alloy. The BSF improves the recombination dynamics at the LFC, as long as excessive damage has not been caused to the surrounding regions [63].

One way to reduce recombination is to incorporate a dopant layer into the volume underneath the rear silicon-metal contact [56]. By firing through a dopant layer, a high concentration of dopant is incorporated into the molten silicon substrate selectively melted by a laser [64].

Because a single laser serves three purposes, the efficiency and quality of the LFC process are restricted. For example, using a laser optimized for dielectric ablation to also alloy aluminum and silicon may result in more damage to the silicon bulk, compared to using separate optimized lasers for ablation and alloying. Considering the varying depths and thicknesses of the material layers and energy doses required to achieve melting, ablation, and alloying, the lasing process and LFC quality could be improved by using multiple lasers with wavelengths and pulse widths optimized for each task.

1.2.2 LFC state of the art

Extensive characterization efforts have led to improvements in LFC processing techniques. LFCs are typically fabricated with nanosecond pulse durations, even though extremely precise and costly control of the process is needed to prevent significant ablation of the aluminum layer. In the last decade, the majority of research groups have studied the laser-firing process with single or multiple nanosecond pulses and wavelengths in the green spectrum. [47], [65]–[67].

In general, results have shown a significant loss of aluminum at high vapor pressures and poor contact between the inner aluminum-silicon eutectic and the metallization on the dielectric passivation [68]–[70]. Since aluminum is needed for the aluminum-silicon alloy to form contact, expulsion of aluminum from the contact area should be avoided. Laser pulses ideally should minimize heating of the aluminum surface, leading to an exploration of lower laser powers and defocused beams [43]. Conversely, millisecond pulse lengths can result in improved melting and mixing of aluminum and silicon, in comparison with shorter wavelength lasers [62]. It is, however, challenging to integrate millisecond lasers into LFC production throughput requirements.

As shown in Figure 6, researchers have explored microsecond pulse durations because they offer the advantage of reduced metal expulsion and can be implemented with diffractive optics to process multiple contacts simultaneously to meet production demands [69]. The longer pulses also enhance the alloying of aluminum and silicon in the contact region and improve the formation of a local BSF, which has been shown to decrease recombination at the contact surface [47], [65].

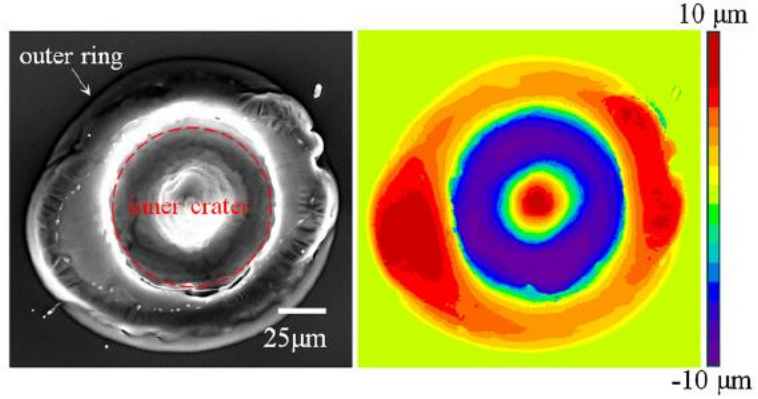


Figure 6 A scanning electron micrograph (SEM) (left) and optical profilometry measurement (right) showing the characteristic inner crater and outer aluminum ring for an LFC fired with a microsecond pulse. [69]

In particular, various parameters using infrared lasers with microsecond pulse durations have been applied and characterized. Such microsecond pulse efforts have correlated aluminum-silicon alloy contact formation with the appearance of a distinct inner crater and outer ring [69]. The regions have been identified as an inner crater where the material first melts under laser irradiation and grows radially with time, based on conductive and convective heat transfer mechanisms. The inner crater is modeled as increasing with fluence. The outer ring region occurs due to the expulsion of aluminum and silicon from the inner crater region [69].

1.2.3 Previous LFC characterization efforts

Thorough understanding of the laser-matter interactions is needed to ensure LFC process control. As a result, LFCs have been extensively characterized since their development in 2002. Multiple research groups have successfully measured devices with LFCs [29], [44]–[46], [50]. Efficiencies as high as 22.4% have been reported, with efficiencies over 18% that have been repeatedly achieved [30], [71]. Device performance with LFCs have been reported using metrics like open circuit voltage, short circuit current, fill factor, and conversion efficiency [49], [72], [73]. Yet deeper understanding of the contacts require further characterization.

Numerous groups have already studied the property-process relationship between a single laser process and electrical properties, composition, and lifetime degradation [32], [60], [61], [65], [70], [74], [75]. Although advanced characterization methods for laser processing exist, the

relationship between laser process, material stack, and electrical performance is still an open research topic in the context of PV. Grohe *et al.* used laser secondary neutral mass spectroscopy and EBIC measurements to evaluate the feasibility of transferring LFC processing onto the industrial scale [46]. Others have attempted to relate the lasing process to electrical properties to predict process control. Kray and Glunz first demonstrated that the passivation layer of LFCs can significantly reduce SRV, then modeled the SRV of any LFC rear side as a function of base doping and contact pitch [47]. Fischer *et al.* developed an analytical model to calculate SRV of point-contacted rear side LFCs [76].

From Fischer's model, Kray and Glunz investigated the relationship between rear-side recombination, contact pitch, and base doping for LFCs [47]. Glunz *et al.* took co-located SEM and EBIC images on LFCs to correlate regions of strong EBIC signal with areas of electrical contact in the LFC [29]. Sanchez-Aniorte *et al.* performed energy dispersive spectroscopy (EDS) and *I-V* measurements of different LFC stack parameters and lasing conditions to identify elemental characteristics of good contact within the parameter space [60]. Urabe *et al.* characterized the extent of laser damage on the passivated silicon bulk using microwave photoconductance spectroscopy (μ -PCD) for lifetime mapping [77]. Raghavan *et al.* used cross-sectional transmission electron microscopy (TEM) to relate laser parameters to morphology, resistance, and composition of LFCs [70]. Raghavan *et al.* later evaluated the influence of changes in microsecond laser processing parameters on contact morphology, resistance, and composition [69]. Glunz *et al.* tested LFCs on *n*-type silicon, using the laser to contact and form the emitter. This demonstrated that LFCs result in a local Al-BSF surrounded by a small damaged layer [78]. Schneiderlochner determined that LFC lasing is not causing deep bulk damage is not contributing to post-lasing lifetime degradation [79].

The bulk of characterization efforts have focused on optimization of the single lasing process and understanding how lasing affects performance. Many aspects of LFC processing still require better understanding. A large reason for this is the difficulty of finding experimental techniques that can match the high resolution (sub-10 μm) and sensitivity of the parameters of interest [67], [75]. Recently, studies using μ -Raman and μ -photoluminescence measurements have identified highly-doped regions in LFCs. Roigé *et al.* was able to correlate these results with conductive-atomic force microscopy measurements to identify the high-conductivity zones in

LFCs, providing submicron detail about contact formation [75]. Measurements at these resolutions and higher can elucidate details about the effects of laser processing that have previously been too difficult to access.

1.3 Current challenges to implementing LFC's in the market

Implementing LFCs for high-efficiency cell architectures requires that LFC processing produces consistent results. This necessitates a full understanding of how lasing affects the structure and properties of a solar cell. Previous characterization efforts described in *1.2.3 Previous LFC characterization efforts* (23-25) have assessed how lasing conditions affect the structure and electrical properties of LFCs.

Recombination remains a challenge to the application of LFCs to industry because the damage caused by excessive laser energy affects the passivation layers and substrate that surrounds each LFC. This can result in defects that act as recombination centers, where generated carriers are lost and thus unable to contribute to the current [56]. At the eutectic interface with silicon, structural defects due to melted and recrystallized silicon are large contributors [59].

The ongoing research in laser processing parameters reflects continuing difficulties in process optimization. It is difficult to predict damage profiles and lifetime degradation. Laser-firing generally involves an infrared laser, and Molpeceres *et al.* has reported that the choice of laser can significantly influence the contact quality [55]. The removal of passivation and melting and recrystallization of silicon introduce defect states for free carriers to recombine [31], [43]. Laser damage to the bulk silicon is an unsolved issue that limits overall cell efficiency. This motivates further exploration of the lasing parameter space to understand how to achieve contact with minimal disorder to the silicon and passivation layers.

The state-of-the-art single laser firing process uses the same lasing parameters for melting metal, dielectric ablation, and eutectic formation. Because one laser must serve three purposes, it is not optimized for any of its functions and likely creates more bulk damage than necessary. Ideally, a small-diameter laser should rapidly deposit a high dose of energy to ablate the dielectric and avoid heating the surrounding material unnecessarily. Another larger-diameter, long laser pulse should be used to encourage metal reflow and mixing with the exposed silicon.

Using one laser requires a compromise between these functions. Raghavan *et al.* established that pulse width influences whether ablation or melting occurs [69], [80]. The absorption depth of laser energy depends on the wavelength of light applied. One laser results in a lasing process that deposits excessive energy into the silicon, causing more material to melt and recrystallize than necessary for contact formation. Lifetime-limiting structural defects are the result, and it remains difficult to predict damage profiles and lifetime degradation. Laser-matter interactions need to be related to the LFC performance and their effects on the bulk substrate.

Attempts to optimize lasing parameters have found that specific contact resistances as low as $.91 \text{ m}\Omega \text{ cm}^2$ for visible lasers and $.57 \text{ m}\Omega \text{ cm}^2$ for UV lasers could be obtained. The suspected reason for this is that the UV laser may absorb more shallowly than the visible laser, generating fewer defects [61].

Optimizing lasing parameters is important for reducing overall damage [55], [60], [81]. The ideal laser process would deposit just enough energy to heat the aluminum until molten, introduce only enough stress to ablate the dielectric layer, then melt the silicon and alloy it with aluminum for contact formation. With a single laser process, the laser that can achieve dielectric ablation is likely more powerful than needed to melt the bulk silicon, resulting in unnecessary damage. Instead of using one laser for tasks that have power requirements, we have tested a two-laser firing process for LFC formation. The two-laser approach could improve over the state-of-the-art because each laser is optimized for a single task (melting vs. ablating), meaning that the minimum energy for each task can be targeted.

1.4 Approach

In my thesis, I hypothesize that a simultaneous two-laser firing process can improve upon the one-laser process by using two task-optimized lasers for dielectric ablation and melting/mixing. The aim is to minimize the amount of energy deposited in the silicon, while achieving eutectic formation. I address the issue of process optimization and LFC characterization by 1) testing a simultaneous two-laser LFC firing process and 2) applying high-sensitivity, synchrotron-based techniques to evaluate elemental constitution LFC on the sub-micron scale and compare these to electrical properties to establish a property-process relationship for different LFC conditions.

Chapter 2 (pgs. 27-31) contains background information about the LFC material stack tested and the structural and electrical characterization techniques. In Chapters

3. Experimental Results (pgs. 31-38) and 4 (pgs. 39-43), I apply these characterization techniques to single-laser and double-laser LFC samples to relate the process to the structural and electrical properties within the chosen parameter space. I also show how synchrotron-based XRF techniques can provide a unique way to characterize the structural properties of LFCs.

The goal is to achieve the same contact quality as a single-laser process, but with less damage. As with a single laser, this two-laser process starts with a 1064 nm microsecond laser that melts the metal surface. As the dielectric is exposed under the molten metal, the 512 nm nanosecond laser is turned on. The 512 nm laser pulses between 35 and 70 times, delivering pulses of energy that introduce thermal stress to ablate the passivation layer. Because the 1064 nm laser is still on, energies can couple so that the 512 nm laser can deposit less energy than in a single-laser process. This minimizes the damage caused below the dielectric. When the dielectric is removed, the 512 nm laser should no longer pulse while the infrared (IR) laser is still on. This IR laser heats the exposed and ideally minimally damaged silicon, as the melted metal reflows into the contact hole for alloying.

2 Methods

2.1 Sample preparation

The processing parameters for this work were chosen from baseline laser energy doses and wavelengths that had been established during previous experiments. For the green laser parameters, the number of pulses per LFC were chosen based on lifetime degradation studies. The pulses per LFC in this work were chosen based on how much lifetime degradation was visible using photoconductance-calibrated photoluminescence, which is a characterization technique discussed in **2.3.1.1 Photoconductance-calibrated Photoluminescence Imaging (PC-PLI)** (pg. 30). The IR lasing conditions were picked based on the lowest energy that resulted in observable metal melting in the microscope. The higher IR lasing conditions were chosen to target incremental structural changes caused by the melting.

The samples were prepared by the Institute of Energy Conversion (IEC), located at the University of Delaware, and IPG Photonics (IPG). IEC fabricated the material stack, consisting of an aluminum-antimony-titanium metal layer, an intrinsic amorphous silicon layer, a silicon nitride passivation layer, an *n*-type crystalline silicon layer, then another amorphous and passivation layer, such that the rear is metallized and the front surface is passivated. The material stack is shown in

Figure 7. The specific thicknesses of the layers are as follows: 150 μm of *n*-type Czochralski crystalline silicon, 8 nm of intrinsic amorphous silicon (i a-Si), 60 nm of hydrogenated amorphous silicon nitride (SiN_x), and metal strips for LFCs made of 5 nm of titanium, 50 nm of antimony, and 500 nm of aluminum. The titanium layer assists adhesion between the antimony and the silicon nitride passivation layer. The antimony serves as the *n*-type dopant for the LFC after firing. The thicker layer of aluminum is used for lateral current conduction [82].

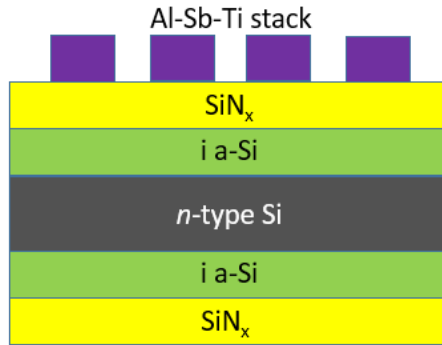


Figure 7 The material stack of the samples used to test different LFC lasing parameters. The layers are not to scale.

Polished and textured *n*-type float zone wafers with 1-5 Ωcm resistivity were used. The textured samples have pyramidal structures of 1-3 μm . Samples were cleaned with Piranha solution (1:30 $\text{H}_2\text{O}_2:\text{H}_2\text{SO}_4$) and HF before the amorphous silicon layers and silicon nitride layers were deposited using plasma-enhanced chemical vapor deposition. Electron beam evaporation was used to deposit the metal stack in strips on the rear side of each sample.

On each sample, four rows and six columns of metallized strips were deposited on the silicon nitride, as shown in Figure 8. Each strip had 5 LFC spots fired on it, with .5 mm spacing. Each row corresponds to a different lasing condition. The lasing conditions were repeated to demonstrate repeatability and to improve accuracy when measuring contact resistance.

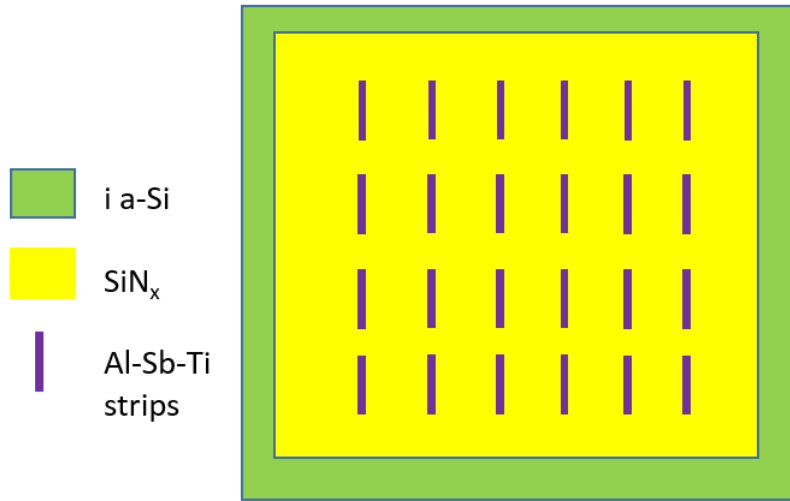


Figure 8 A diagram showing the rear of the sample. Individual LFC spots were fired into the metallized strips. Each row corresponds to a new lasing condition. The dimensions are not to scale.

2.2 LFC Lasing Parameters

Different combinations of two lasers of different wavelengths were tested. The first laser was a 532 nm (“green”) fiber laser manufactured by IPG Photonics. The pulse width was set at 1 ns and the pulse energy was 2.8 μJ . The green laser fired each spot multiple times, either 35 or 70 times. The beam was defocused to 650 μm . The second laser was a 1070 nm (“IR”) fiber laser also manufactured by IPG Photonics. Two pulse widths, 46 and 50 μs , were used to result in pulse energies of 140 and 400 μJ , respectively. The IR laser was only fired once. The 46 μs (140 μJ) IR lasing parameter was chosen because it was the minimum energy dose at which visible melting of the metal stack was achieved. The parameters are listed in Table 1.

Laser wavelength	Pulse width	Pulse energy (μJ)	Pulses per LFC	Energy (μJ)
532 nm (Green)	1 ns	2.8	35	98
	1 ns	2.8	70	196
1070 nm (IR)	46 μs	140	1	140
	50 μs	400	1	400

Table 1 A summary of the four lasing parameters used to fire LFCs in this study.

2.3 Characterization Techniques

2.3.1 Electrical Characterization

2.3.1.1 Photoconductance-calibrated Photoluminescence Imaging (PC-PLI)

Two of the typical methods to measure minority carrier lifetime in silicon employ PCD and photoluminescence (PL). The photoconductance tool used in this work was the Sinton Instruments WCT-120. This measurement system comprises of a flash lamp, a calibrated light sensor, and a radio frequency (RF) coil. A sample is measured by placing it on the RF coil, then using the flash lamp to generate a broadband light source that faces the sample. This flash excites carriers in the sample, and the carriers induce a voltage in the RF coil. The voltage is recorded as a function of time, while the light sensor measures the incident photon flux to determine the injection level. The output data consists of the apparent lifetime across the measured injection range [83].

Photoluminescence (PL) measurements can be performed as a transient measurement or as a quasi-steady-state (QSS) measurement that uses a charge-coupled device (CCD) camera. In the transient approach, carriers are pumped into an excited state. Lifetime is proportional to the intensity of the luminescence signal, which relates to how much radiative recombination is occurring in the material. In the QSS approach, which is commonly used for silicon, the sample is uniformly illuminated with a single wavelength above the bandgap of the material. A CCD camera images luminescent photons in space [84].

With this QSS approach, the measured luminescence intensity must be calibrated to the excess carrier density or lifetime of the material. Photoconductance calibration and self-consistent calibration have both been used to convert luminescence intensity into lifetime values [85], [86]. In QSS-PL, the generation rate across the sample is constant while the measured injection level could vary. Multiple images must be taken at a range of illumination laser powers to specify an injection-dependent lifetime curve.

Contrast was used to evaluate change in sample lifetime after lasing. Over regions with consistent peaks and valleys of PL signal, which correspond to unlased and lased regions, points were selected to measure intensity. I_{in} indicates the intensity of a spot in the valley that is visibly within the darkened lased region of lower lifetime. I_{out} indicates the intensity of an unlased spot, outside the darkened region.

$$Contrast = \frac{I_{in} - I_{out}}{I_{out}} \quad \text{Eq. 4}$$

Here, positive contrast values correspond to lifetime degradation. Photoluminescence is used to evaluate minority carrier lifetime, τ_{eff} , such that a lower PL signal corresponds to shorter lifetimes [84]. Two terms contribute to the value of τ_{eff} . One is a bulk lifetime term, τ_{bulk} , which describes the minority carrier lifetime in the bulk of the material. In the bulk, carriers recombine by the mechanisms described in Section

μ -XRF data collection can occur using a step-by-step mode (“stepscans”) or a newly-implemented on-the-fly mode (“flyscans”). With stepscans, the sample must be measured and shifted to collect fluorescence data at each pixel, until a map of pixels is formed. This incremental shifting requires approximately 300 ms per pixel of additional “settling” time. The advantage of flyscans is that the sample continuously moves while the detector continuously collects data. As a result, flyscans avoid the 300 ms per pixel stepscan overhead and enable faster scanning of samples. Given the same stepscan time, flyscans can map larger areas while maintaining the same sensitivity, and can scan an area ten times faster than a stepscan by halving sensitivity [95].

3. Experimental Results

The effect of a two-laser simultaneous process was evaluated before and after processing by observing the structural and electrical characteristics of LFC material stacks after processing.

3.1 PL Images

All PL imaging was performed using the 808 nm diode laser and a Princeton Instruments PIXIS 1024BR camera, which was fitted with an indium phosphide wafer and a Schott RG1000 long-pass filter. The Sinton Instruments WCT-120, an offline wafer-lifetime measurement tool, was used to calibrate the PL images [85]. A Czochralski silicon sample of similar thickness, reflectivity, and resistivity to the LFC samples was used to determine the calibration parameters. The sample thickness was 150 μm , reflectivity was .12, and doping was $3 \times 10^{15} \text{ cm}^{-3}$, based on the QSSPC resistivity estimate of $1.5 \Omega\text{-cm}^2$. The setup did not correct for lateral carrier diffusion due to inhomogeneous excess carrier densities, photon scattering or reabsorption within the sample, or photon spreading within the sensor [96]. Without correction, lateral carrier diffusion can affect the spatial information of the measurement.

First, the minority carrier lifetime of each sample was measured before laser processing. The lifetimes were taken using the set-up described above, and the sample lifetime was calculated as the average of lifetimes over a 300-pixel circle centered in the image. Laser power percentage was varied between 10% and 60% to find a setting that produced optimal PL images. The images of lased samples in Table 2 were taken with 40% laser power and contrast values were used to evaluate lifetime degradation.

After laser processing, PLI linescans were taken down a column on each sample, as seen in Figure 9 (b). As seen in Figure 9 (c), each linescan plot shows lifetime values as a function of position on either the x - or y -axis. Post-lasing lifetime degradation was evaluated by calculating the contrast between the lased line and the un-processed area around each lased line. Contrast values were calculated in terms of arbitrary units (a.u.) in MATLAB by loading each PL image and the accompanying PL data, manually selecting 30 points within an LFC on a strip, and then selecting 30 points right outside the metal strip. The first 30 points provide lifetime values for laser-degraded material, and the second 30 points provide lifetime values for unprocessed material. For the 30 data pairs, contrast was calculated according to Equation 5. The means of the 30 calculated contrast values are shown for each lasing condition in Table 2.

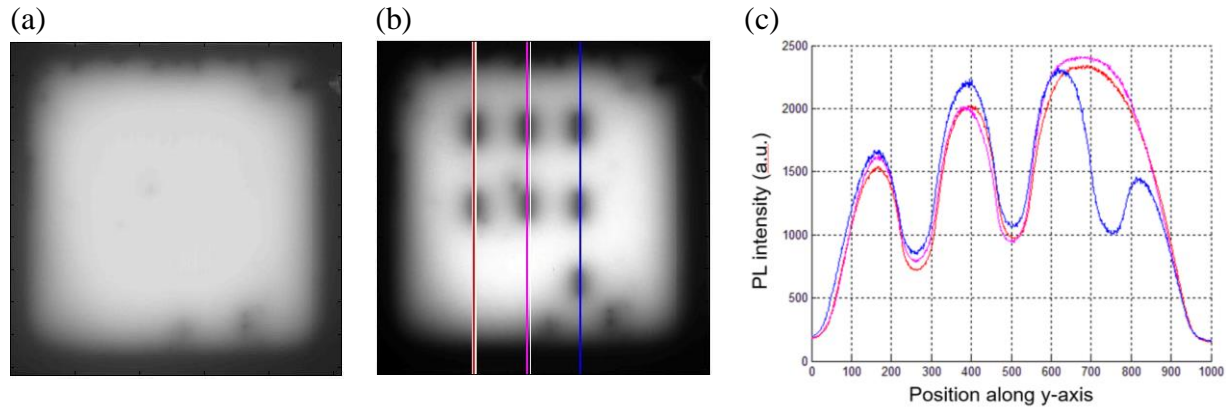


Figure 9 PL images of one sample taken (a) before laser processing, (b) after lasing processing with sampled linescans shown in color, and the corresponding plot of PL intensity shown for the linescans.

Lasing condition	Group 1		Group 2			Group 3		
	Green 1	Green 2	IR 1	Green 1 + IR 1	Green 1 + IR 2	IR 2	Green 2 + IR 1	Green 2 + IR 2
Energy dose ($\mu\text{J}/\text{cm}^2$)	98	196	140	238	336	400	498	596

PL contrast (a.u.)	.067	.062	.10	.092	.11	.15	.16	.16
PLI maps after lasing								

Table 2 Contrast values for different lasing conditions. The groups and condition names refer to those described in Table 1.

3.2 Transmission line measurements of specific contact resistance

R_C was measured using TLM. The resistance values are shown in Table 3. For each sample, five sets of data were used to approximate a linear fit to determine specific contact resistance. The sets of data were taken by measuring the resistance between strips. For example, one set of data measured the resistance between Strip 1 to Strips 2-6, the second set of data measured the resistance between Strip 2 to Strip 1 and Strips 3-6, and so on.

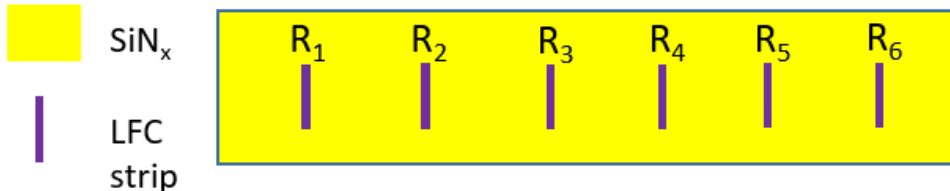


Figure 10 A row of LFC strips that is used for TLM measurements. One data set corresponds to the resistance measurements between one strip and every other strip.

For the samples only fired with a “green” laser, no ohmic contact was measurable between any of the strips. The standard error, $1.5 \text{ m}\Omega \text{ cm}^2$, was approximately the same for the non-infinite R_C measurements. The measured R_C and length between the two measured LFC strips were entered into Microsoft Excel, then the “STEYX” function was used to calculate the error of the linear regression.

Lasing condition	Green 1	Green 2	IR 1	Green 1 + IR 1	Green 2 + IR 1	IR 2	Green 1 + IR 2	Green 2 + IR 2
------------------	---------	---------	------	----------------	----------------	------	----------------	----------------

Energy dose ($\mu\text{J}/\text{cm}^2$)	98	196	140	238	498	400	336	596
R_C ($\text{m}\Omega\text{cm}^2$)	∞	∞	$<13.5 \pm .73$	$<6.7 \pm .73$	$<8.7 \pm .73$	$<8.9 \pm .73$	$<8.5 \pm .73$	$<6.8 \pm .73$

Table 3 R_C for different lasing conditions as measured by TLM. The condition names refer to those described in Table 1. Standard error for all non-infinite R_C measurements was approximately .73 $\text{m}\Omega\text{ cm}^2$.

3.3 μ -X-ray fluorescence spectroscopy for elemental mapping

After lasing, spatially-resolved μ -XRF measurements were taken of a single LFC for each condition. The flyscan mode allowed us to determine elemental composition with unprecedented levels of sensitivity, resolution, and speed. All elemental channel maps and the Si:Al map are shown in Table 4. The scale bar indicating elemental counts is in \log_{10} , so 15 actually indicates 10^{15} counts detected.

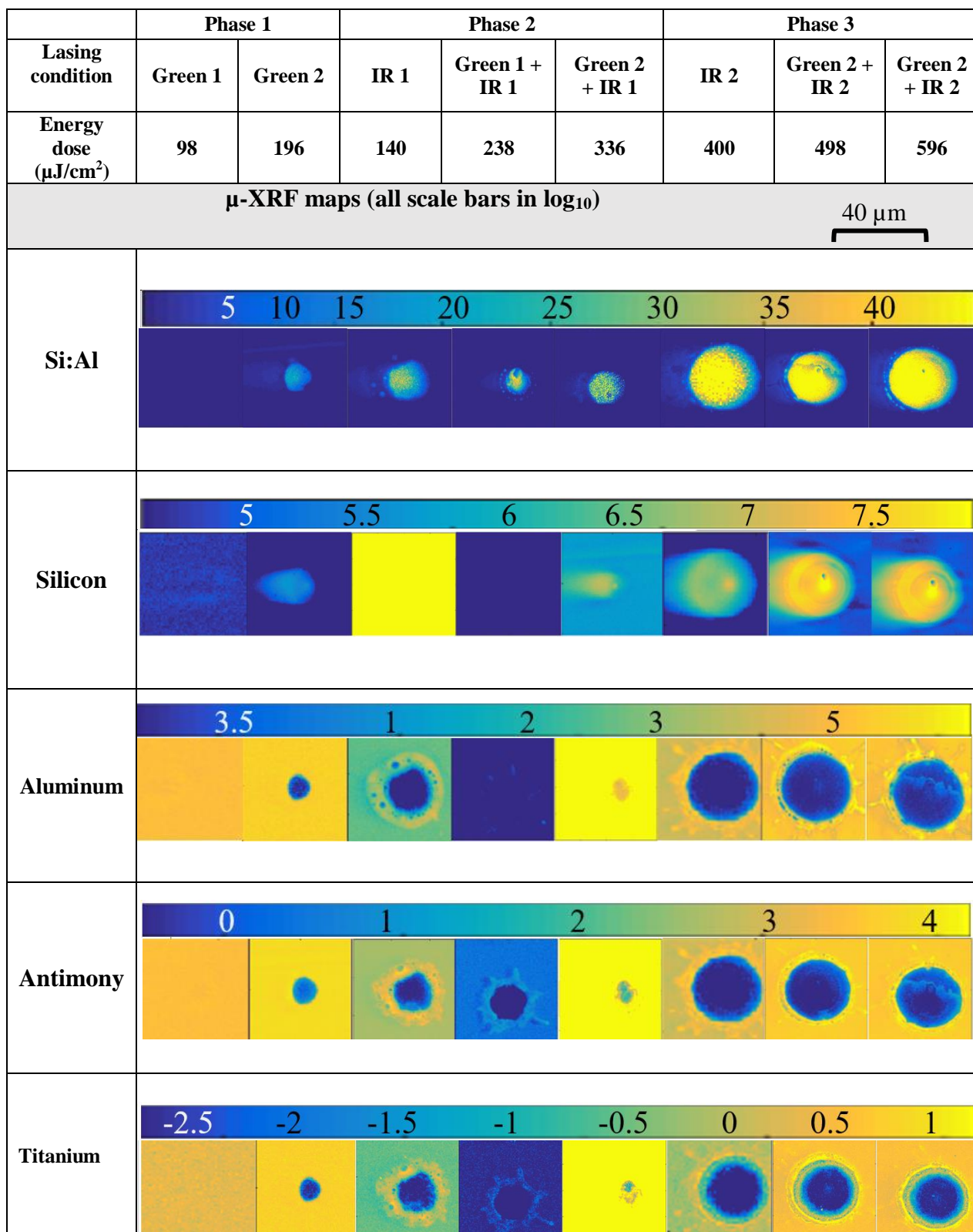


Table 4 $\mu\text{-XRF}$ maps showing counts for silicon, aluminum, antimony, titanium, and Si:Al for LFCs fired with the described lasing conditions.

All silicon maps contain a smear to the left of the image. This is an artifact caused by the incident X-ray beam hitting the sample at an angle. Since the silicon channel was used to calculate Si:Al, some Si:Al maps also contain the artificial smear.

In general, the ROIs show aluminum, titanium, and antimony counts outside a large central hole and predominantly silicon counts within the hole. To facilitate discussion of the LFCs, three contact formation phases have been defined for comparison. As first described in **2.2 LFC Lasing Parameters**, Group 1 refers to the two smallest LFCs that are formed using “Green 1” and “Green 2” lasing conditions. Group 2 refers to three LFCs that use the 140 μJ IR pulse: “IR 1,” “Green 1 + IR 1,” and “Green 2 + IR 1”. Group 3 refers to the three largest LFCs that use the 400 μJ IR pulse: “IR 2,” “Green 1 + IR 2,” and “Green 2 + IR 2.”

For Group 1, “Green 1” shows silicon counts. With the scales used, “Green 1” does not show significant elemental differences between un-lased and lased regions. The “Green 2” map shows higher metal counts in a ring surrounding a high-silicon count hole. For Group 2, the samples show rings of high metal counts and a cavity that is high in silicon counts only. For Group 3, three distinct features of each LFC are visible. There is an outer ring with a splatter pattern that contains high metal counts. Within the outer ring, there is another ring that is most apparent in the titanium channel. Lastly, the central hole is metal-poor and silicon-rich.

MATLAB was used to define an area in each Si:Al map and calculate the average Si:Al value within a uniform section of the LFC. These average Si:Al values are shown in Table 5.

Lasing condition	Phase 1		Phase 2			Phase 3		
	Green 1	Green 2	IR 1	Green 1 + IR 1	Green 2 + IR 1	IR 2	Green 2 + IR 2	Green 2 + IR 2
Energy dose ($\mu\text{J}/\text{cm}^2$)	98	196	140	238	336	400	498	596
Si:Al	1.01	13.4	24.5	23.0	29.1	55.1	63.8	61.9

Table 5 The Si:Al values for each of the lasing conditions, as determined from the μ -XRF maps

3.4 SEM and EDS

SEM images were taken for each processing condition to evaluate the structural characteristics of the LFC. The same LFC was used for the EDS and μ -XRF studies to correlate elemental and structural features.

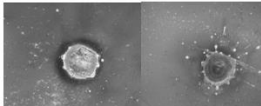
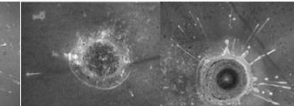
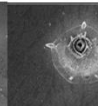
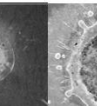
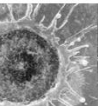
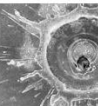
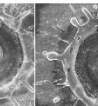
	Phase 1		Phase 2			Phase 3		
Lasing condition	Green 1	Green 2	IR 1	Green 1 + IR 1	Green 2 + IR 1	IR 2	Green 2 + IR 2	Green 2 + IR 2
Energy dose ($\mu\text{J}/\text{cm}^2$)	98	196	140	238	336	400	498	596
SEM images								

Table 6 SEM images showing contacts that were fired with each lasing condition.

The SEM images are shown in Table 6. In Phase 1, the “Green 1” condition resulted in a solid formation with small splatter features at the edge. “Green 2” appears similar to Green 1, but with larger splatter features and surrounding droplets. In Phase 2, the rings seen in the XRF maps are also visible in the SEM images. The two conditions that include Green pulses include a spot in the center of the contact. In Phase 3, all contacts show a ring with splatters extending outward. The “IR 2” condition has an amorphous interior, in comparison to the “Green 1 + IR 2” and “Green 2 + IR 2” conditions that exhibit small craters and pool-like formations

EDS was taken for “IR 2” sample to examine its elemental distribution. Higher color saturation indicates greater elemental counts, while black indicates that the element was not detected.

4. Discussion

The aim of this work is to characterize the principal differences between single-shot and double-shot lasing processes and to determine how each process can improve LFC quality. An ideal LFC should include at least (1) a metal-silicon interface for low R_C and (2) a small lased contact area to minimize recombination and minority carrier lifetime degradation [97].

In this section, the experimental results presented in Chapter 3 (pgs. 31-38) are correlated to identify relationships between the lasing process and LFC properties, like the metal-silicon interface and the lifetime characteristics listed above. The unique combination of lifetime information from PC-PLI, elemental mapping using μ -XRF, R_C values from TLM, and micrographs from SEM combine structural and electrical properties that can be related to the range of tested processes. Characterization of the double-shot lasing processes, which have not been

tested in literature before, provides insight into whether LFC production can be optimized. With the sensitivity and resolution of the μ -XRF maps, the microstructure of LFCs can be studied at an unprecedented level for both single- and double-shot lasing processes.

The results in this work pertain to a sample set of six conditions, where each condition is a unique lasing process. With these six conditions, a comparison was possible between single-lasing conditions, which include “Green only,” “IR only,” simultaneous double-lasing conditions, which include “Green + IR.” For these conditions, the impact of increasing the green and/or IR condition on structure, electrical properties, and lasing process was observed. These results suggest that a “Green + IR” process could possibly produce a superior LFC to single lasing conditions, but cannot conclude what conditions are optimal. Ideally, a parameter sweep of both the “Green” and “IR” lasing conditions would have been conducted to determine the result of incremental process change. A parameter sweep would also provide further evidence to confirm the structure-property-process relationships that these results suggest.

Furthermore, the R_C TLM data have represent upper bounds, and were repeatable only for textured samples, but not for polished samples. R_C is one of the determining factors of an effective LFC, which limits the conclusions that can be drawn about structure-property-process relationships.

The data is presented in the same groups (Group 1, Groups 2, Group 3) described in 3.1 **PL Images** (pg. 31) and addressed as two optimization problems.

- 1) LFC process optimization in 4.1, by examining single-shot and double-shot lasing
- 2) LFC characterization optimization in 4.2, by using μ -XRF as a tool for evaluating LFCs (via the Si:Al ratio, as an indicator of contact formation)

To discuss process optimization, the lasing process will first be reviewed to emphasize the goal of the experiment. In section 4.1, the structure-property-process relationships will be discussed, beginning with how the lasing process impacts lifetime degradation (PLI data) in 4.1.1, R_C in 4.1.2, and elemental distribution in 4.1.3. In 4.1.4, these results are summarized and suggestions are made about how to improve LFC processing. To discuss LFC characterization in sub-section 4.2, the EDS data and μ -XRF data are compared to show that μ -XRF may provide an alternate quantitative measure of contact quality.

4. Discussion

4.1 Expected property-process relationships of two-laser firing

The two-laser firing sequence tested in this work was chosen based on existing literature and discussion with lasing experts, which suggested that LFC formation in our samples likely occurs as follows. The material stack shown in Figure 17 can be used for reference.

- 1) Incident laser energy (a combination of green and IR) heats the metal surface
- 2) The metal melts, boils, splatters externally. The repeated green laser pulses push molten metal outward.
- 3) The dielectric layer beneath is exposed. This dielectric is invisible to the IR laser light [98].
- 4) The laser heats trapped hydrogen in the amorphous silicon layer.
- 5) The trapped hydrogen gas bubbles expand with heating, bubbles up, and peels the layers above. This creates a crater in the dielectric that exposes silicon that has been heated and damaged [97], [98].
- 6) Molten metal reflows into the crater and mixes with the heated silicon, ideally forming a eutectic [58], [62].
- 7) The surface recrystallizes [57], [62], [99].

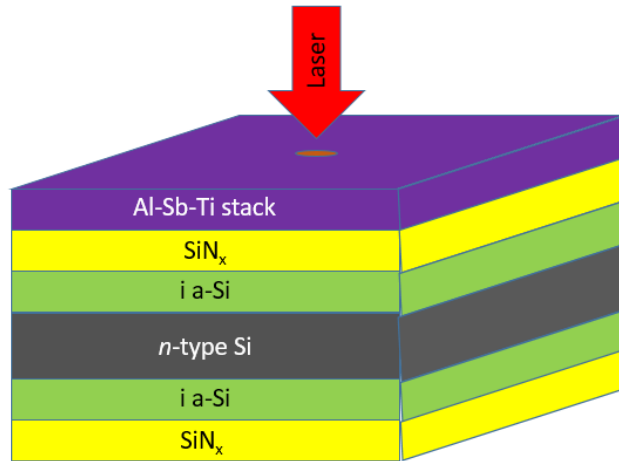


Figure 11 The material stack of the samples used to test different LFC lasing parameters, with the incident laser and lased region shown. The layers are not to scale and the thicknesses are listed in 2.1 *Sample preparation*(pg. 27).

Using the two “Green + IR” firing, the hypothesis is that a lower-energy IR pulse will be needed than for the single laser -firing IR case. Instead, the green and IR laser energies will couple

in Steps (1)-(4). While the lower-energy IR pulse acts as a heat lamp, the nanosecond green laser fires such that the massive injection of energy is deposited too fast to be dissipated before the next pulse. The deposited energy is likely restricted to a small area. The green laser is also absorbed too shallowly to affect the bulk silicon, so coupled energy will only affect metal and the amorphous layer. After hydrogen expansion and dielectric lift-off, the green laser turns off and the IR laser performs Step (6). Coupled with the green laser, the IR laser does not need to be excessively powerful to do Steps (1)-(4). The last melting and mixing step can be achieved with a lower-energy IR pulse. Coupling these lasers could consequently result in less damage to the bulk.

4.2 Structure-property-process relationships

4.2.1 Property-process relationship: PLI measurements

As described in 1.1.2, minority carrier lifetime is an important parameter that plays a role in defining how efficiently a solar cell can operate. During the LFC process, lasing introduces defects that can increase recombination and decrease lifetime. It is important to understand how to efficiently manufacture LFCs while maximizing performance parameters like lifetime. PLI contrast can be used as a measure for lifetime degradation, assuming that the area outside of the lased region is uniformly high, as outlined in 2.3.1.1.

The results in 3.2.2 are plotted against R_C in Figure 12, which indicates that PLI contrast increases from Group 1 through Group 3, but does not vary significantly between lasing conditions in this phase. The green laser may not have a significant impact on lifetime, while lifetime worsens as IR energy dose increases for each group. This suggests that lifetime degradation predominantly depends on the IR laser, and the induced melting and alloying has the greatest impact on lifetime. The green laser, which is meant to ablate the dielectric, likely only damaged the top layers of the LFC stack without impacting the underlying silicon.

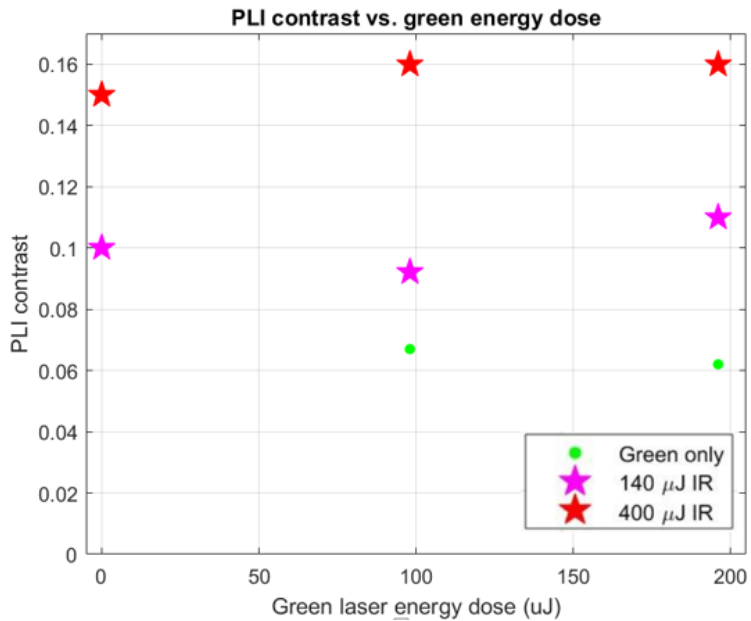


Figure 12 A plot of PLI contrast values versus the green laser energy dose, showing that PLI contrast primarily depends on the IR laser.

Although energy dose increases within each lasing group, there is no observed relationship between PLI contrast and the laser energy doses. The larger-sized LFCs, however, corresponded to greater lifetime degradation. One reason for this could be that a greater surface area has been laser-damaged.

As shown in Table 7, both “IR 1” and “IR 1 + Green 1” SEM images show that the LFCs are approximately the same size. Their PL contrast values are also similar, even though the energy doses are different. The “IR 2” SEM image shows that the LFC diameter is approximately 35% larger than the other two LFCs, and the PL contrast is approximately 50% greater. The PLI results indicate that the IR lasing step causes the highest lifetime degradation, and that the overall lifetime is improved because a smaller fraction of the sample is lased. This supports the hypothesis that a double-shot LFC process could produce better contacts than a single-shot process because lower-energy lasers could be used that minimize the laser-affected area. Future experiments can confirm this by conducting a thorough parameter sweep of green and IR lasing conditions to compare the size and lifetime degradation of “Green + IR” conditions with single lasing conditions.

Condition	“IR 1”	“IR 1 + Green 1”	“IR 2”
Energy dose (μJ)	140	238	400
SEM image 20 μm			
LFC diameter (μm)	22	23	30
PL contrast	.10	.092	.141

Table 7 SEM images of larger LFC and smaller LFCs, along with the diameter and the PL contrast values.

4.2.3 Property-process relationship: TLM measurements

An ideal electrical contact for a solar cell should minimize losses that occur due to defects that are formed at the silicon and the metal eutectic. For optimal electrical properties, LFC processing parameters should aim to minimize R_C values.

To relate the electrical properties of the LFCs to the process, the TLM values were plotted against lasing parameters, as shown in Figure 13. Group 1 was not plotted because no measurable contact was formed. The plotted data points do not indicate that a simultaneous firing condition would lead to improved LFC R_C values over a process that only uses an IR laser alone. Considering the standard errors for each measurement, there is no significant difference between the R_C values.

In these samples, a green laser alone could not achieve contact for an LFC stack and it is not clear whether a simultaneous firing condition is advantageous. Since R_C was only measurable LFCs that used an IR laser, it seems that the IR is critical for contact formation. This indicates that for a range of green laser conditions, simultaneous firing with IR is superior to single lasing. To explore the full parameter space where “Green + IR” is optimal, future experiments should retest single-shot and double-shot LFCs using lower IR energy doses, as the ones tested here may already be too powerful for optimal contact formation.

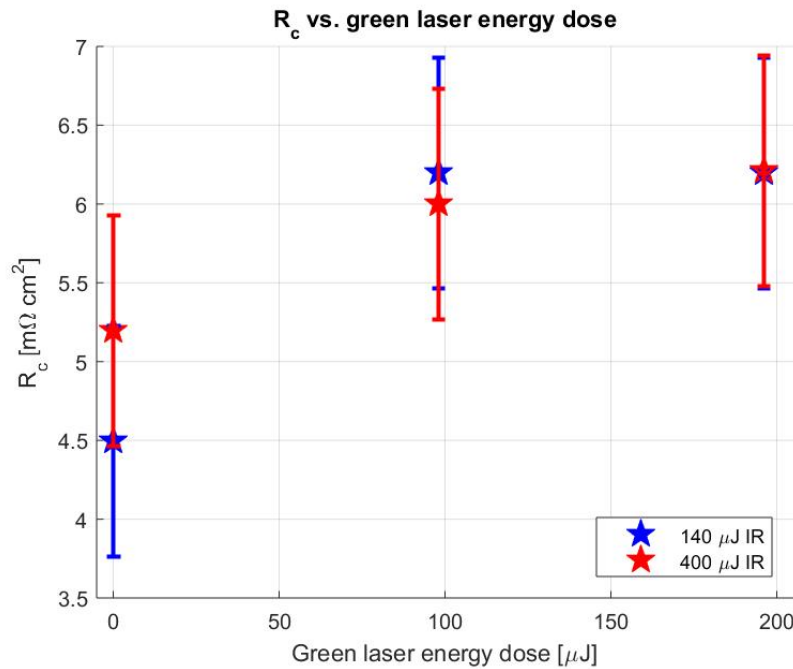


Figure 13 The R_c data from Table 3 plotted against green energy dose. Group 2 corresponds to the red symbols, and Group 3 corresponds to the blue symbols. Group 1 is not shown because contact was not measured.

4.2.2 Structure-property-process relationship

In this section, the SEM micrographs, shown in Table 6 (pg. 37), are analyzed in context of the SEM, μ -XRF, PLI, and TLM R_c values to elucidate the relationship between the LFC structure, the lasing process, and electrical properties. The quantitative data from this work are listed in Table 8. The correlation of these SEM micrographs with R_c values can indicate structural elements that correspond to optimal electrical properties and optimal processing parameters. The effects of lasing are not fully understood yet, making it difficult to optimize LFC processing. The aim of this work is clarify these relationships, so the characteristics of a high-quality LFC can be identified and manufactured.

In this section, high-resolution studies of LFC elemental composition from μ -XRF can also provide unprecedented information about laser-matter interactions, such as the location of contact formation, structural uniformity, and metal distribution. This information can be used for LFC process optimization by determining the physical characteristics that predict LFC performance. Then, SEM micrographs were used to understand how different green and IR lasing parameters

resulted in structural characteristics. This provided insight into which laser achieved which step of the LFC process and how to optimize it.

The lasing conditions, groupings, and data introduced in Chapter 3 (pgs. 31-39) are repeated below in Table 8, and the structural characteristics will be discussed next for each group.

	Group 1		Group 2			Group 3																		
Lasing condition	Green 1	Green 2	IR 1	IR 1 + Green 1	IR 1 + Green 2	IR 2	IR 2 + Green 1	IR 2 + Green 2																
Energy dose ($\mu\text{J}/\text{cm}^2$)	98	196	140	238	336	400	498	596																
PLI contrast	.067	.062	.10	.092	.11	.15	.16	.16																
R_C ($\text{m}\Omega \text{ cm}^2$)	∞	∞	<13.5	<6.7	<8.5	<8.9	<8.7	<6.8																
Si:Al	1.01	13.4	24.5	23.0	29.1	55.1	63.8	61.9																
Plot of normalized data	<p>A bar chart comparing normalized data for three groups (Group 1 in red, Group 2 in blue, Group 3 in green) across three metrics: PLI contrast, Contact resistance, and Si:Al. The Y-axis ranges from 0 to 3. For PLI contrast, Group 1 is ~0.4, Group 2 is ~0.7, and Group 3 is ~1.0. For Contact resistance, Group 1 is ~3.0, Group 2 is ~1.0, and Group 3 is ~0.8. For Si:Al, Group 1 is ~0.1, Group 2 is ~0.4, and Group 3 is ~1.0.</p> <table border="1"> <thead> <tr> <th>Metric</th> <th>Group 1</th> <th>Group 2</th> <th>Group 3</th> </tr> </thead> <tbody> <tr> <td>PLI contrast</td> <td>~0.4</td> <td>~0.7</td> <td>~1.0</td> </tr> <tr> <td>Contact resistance</td> <td>~3.0</td> <td>~1.0</td> <td>~0.8</td> </tr> <tr> <td>Si:Al</td> <td>~0.1</td> <td>~0.4</td> <td>~1.0</td> </tr> </tbody> </table>								Metric	Group 1	Group 2	Group 3	PLI contrast	~0.4	~0.7	~1.0	Contact resistance	~3.0	~1.0	~0.8	Si:Al	~0.1	~0.4	~1.0
Metric	Group 1	Group 2	Group 3																					
PLI contrast	~0.4	~0.7	~1.0																					
Contact resistance	~3.0	~1.0	~0.8																					
Si:Al	~0.1	~0.4	~1.0																					

Table 8 The tested lasing conditions are categorized into Group 1, Group 2, and Group 3 depending on the IR energy dose used. Data for all quantitative measurements (R_C , PLI contrast, and Si:Al) are normalized and shown in the bar chart.

Group 1—“Green 1” and “Green 2”

As discussed in 4.1.1, no contact was measured for Group 1, which indicates that insufficient silicon-aluminum alloying has occurred for these “Green only” conditions. In Table 9 (45), the SEM images and μ -XRF maps indicate that splattering features correspond to metal that has been expelled from the lased region, but these features do not indicate alloying.

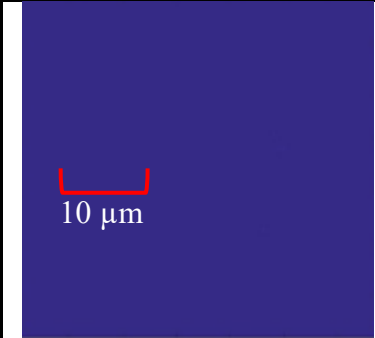
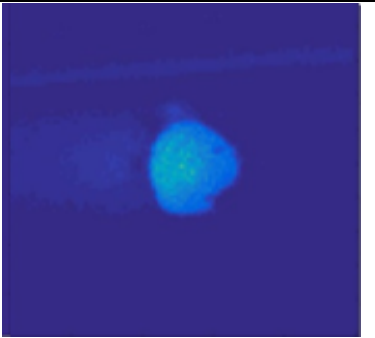
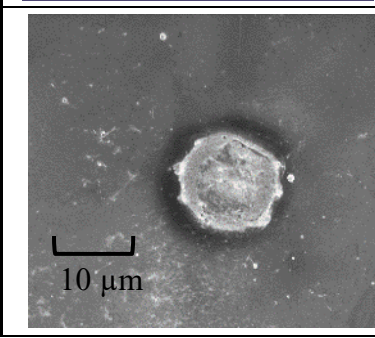
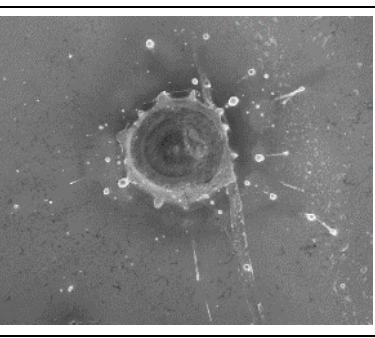
Lasing condition	Green 1	Green 2
PLI contrast	.067	.062
Si:Al	1.01	13.4
Si:Al μ-XRF maps		
SEM images		

Table 9 Data for Group 1, along with SEM images and XRF maps, previously shown in Table 4 μ -XRF maps showing counts for silicon, aluminum, antimony, titanium, and Si:Al for LFCs fired with the described lasing conditions.(35), Table 6 (37), and Table 8 (44)

The lower Si:Al values may indicate a lasing process that deposits sufficient energy to ablate the metal and passivation layers above the silicon, but not enough energy for the melting and mixing needed to produce the metal-semiconductor eutectic. This points toward the possibility of correlating LFC properties to Si:Al so it can be used as a measurable quantity to judge LFC performance. It was expected that the nanosecond green pulses likely prevented the wide-area heating and melting needed for contact formation [100].

From the μ -XRF maps in “Green 1,” shown in Table 9 (pg. 45), the area above the splatter ring consists of metals. The ring of high metal counts indicates that not all the expelled metal reflowed to the center before cooling. This further suggests that the green laser performed as expected, with the nanosecond pulse heating a local area and ablating the material there. As the rapid energy deposition limits the thermal diffusion of energy away from the lased area, the laser energy may have caused metal to melt and boil in a contained area, then splatter outward to expose the dielectric beneath. Subsequent laser pulses likely induced Steps (4) and (5) of the lasing sequence described in Chapter 4 (pg. 39).

Unlike “Green 1,” the μ -XRF map for “Green 2” in Table 9 (pg. 45) shows high metal counts everywhere except the center, where a 10:1 ratio of Si:Al and low nitrogen counts indicate the SiN_x passivation layer was at least partially exposed. Considering the low Si:Al counts in the “Green 1” center hole, it is unlikely that enough energy was deposited during Steps (4) and (5) to peel off the dielectric. The low PLI contrast values support that the dielectric remained in place, as the passivating layer preserved the lifetime in the lased area.

Using these green conditions did not result in contact formation because it is unlikely that metal-silicon alloying occurred, as suggested by the PLI contrast and structural characteristics. A higher green energy dose may be needed for contact formation, but a simultaneous IR laser could also be added so that the coupling of two lower-energy lasers could provide enough energy for dielectric ablation. Such coupling is explored in the next two sections, Group 2 and Group 3.

Group 2—“IR 1,” “IR 1 + Green 1,” “IR 1 + Green 2”

The samples in Group 2 may indicate that the IR laser improves contact formation by increasing alloying. The measurable R_C values are accompanied by larger Si:Al values, which indicate that more silicon has been exposed than in Group 1 and that sufficient alloying has been achieved.

In Table 10 (pg. 47), the “IR 1” pulse appears to cause the larger ring that appears throughout Group 2, and the squiggly pattern of the center hole indicates silicon that was melted then quickly re-solidified. The presence of re-solidification is supported by the approximately 50% PLI contrast value, which suggests lifetime degradation due to defects in the recrystallized surface. Steps (1) through (4) (pg. 39) were likely achieved as the IR laser caused the metal to melt, and the thermal energy pushed the molten metal to the outside to form the ring. The addition of green lasers in “IR 1 + Green 1” and “IR 1 + Green 2” result in smaller craters that appear in the SEM.

	“IR 1”	“IR 1 + Green 1”	“IR 1 + Green 2”
PLI contrast	.10	.092	.11
Si:Al	24.5	23.0	29.1
R_C ($\text{m}\Omega \text{ cm}^2$)	<13.5	<6.7	<8.5

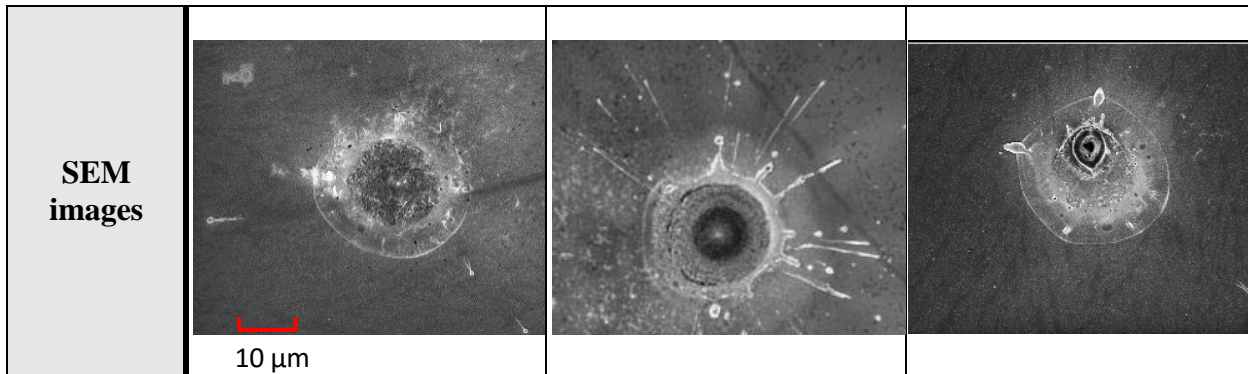


Table 10 Selected SEM micrographs and data of Group 1 conditions, previously shown in Table 6 (37).

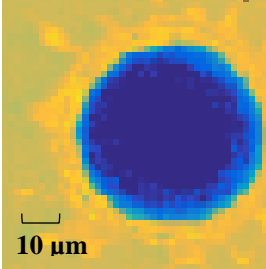
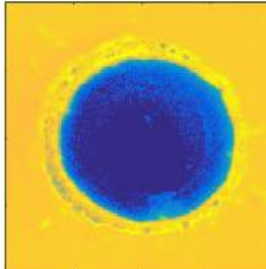
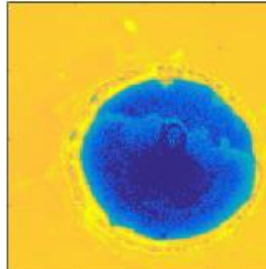
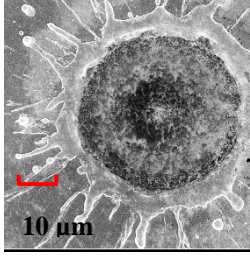
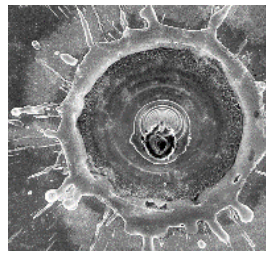
In the “IR 1” condition, the high Si:Al counts and finite R_C value suggest that the IR removed the dielectric, melted the silicon, and achieved alloying with aluminum. “IR 1” achieved an Si:Al value of 24.5, double that of “Green 2” and with less energy deposited. The R_C value indicates that the lasing process formed contact by exposing enough silicon and mixing it with aluminum to form a eutectic. For LFC formation, “IR only” was likely more effective than “Green only” because it uses microsecond pulse widths, as the longer lasing time could heat the metal and expose silicon without ablating much material. Additional heating may have also facilitated subsurface melting of the exposed silicon, which can improve alloying with aluminum. “IR 1” deposited less energy than “Green 2,” which suggests that the timescale of the LFC process contact may have a greater impact than the energy dose.

Compared to “IR 1,” simultaneous “Green + IR” conditions exhibit similar Si:Al values and R_C values. It makes sense that the additional green laser does not alter the Si:Al ratio significantly, as the green laser predominantly ablates layers of material. The TLM results in Table 10 (pg. 47) are not precise enough to indicate whether simultaneous firing is superior, so further tests must be done to evaluate R_C .

Since the “IR 1” condition achieved contact without any additional lasers, it is unclear whether the simultaneous “Green + IR” lasing is advantageous. The three conditions of Group 1 all have similar TLM and PLI values, indicating that electrical performance (lifetime degradation and R_C) is not improved with the addition of the green laser and that IR lasing is superior to green lasing for LFCs for these conditions. This suggests that the longer timescale of IR lasing plays an important role in contact formation, specifically for alloying. Still, “Green + IR” may improve LFC performance for different lasing conditions. In the next section, a higher IR dose is tested for “Green + IR.”

Group 3—“IR 2,” “IR 2 + Green 1,” “IR 2 + Green 2”

The data in Group 3 provides further evidence that Si:Al can indicate contact quality and location, but it remains unclear whether “Green + IR” is advantageous for lasing. Compared to the values in Group 2, the Group 3 Si:Al are 2.5x larger and indicate that a greater proportion of silicon was exposed and damaged. The PL contrast values supports this, as there is 57% average lifetime degradation in Group 3, versus 30% average degradation in Group 2.

	Group 3		
Lasing condition	IR 2	IR 2 + Green 1	IR 2 + Green 2
Energy dose ($\mu\text{J}/\text{cm}^2$)	400	498	596
PLI contrast	.15	.16	.16
R_C ($\text{m}\Omega \text{ cm}^2$)	<8.9	<8.7	<6.8
Si:Al	55.1	63.8	61.9
Si:Al μ -XRF maps			
SEM images			

As in Group 2, Group 3 exhibits high Si:Al values along with a finite R_C . These measurements were not significantly changed by the addition of the green laser, as seen in Table 11, which suggests the amount of exposed silicon depends most on the IR contribution. This is suggests that the green laser did not expose additional silicon, as it may have hit where the IR laser had already exposed silicon.

From the SEM images and μ -XRF maps in Table 11, the coupling did not lead to improved alloying or less surface damage. It is possible that the 400 μJ was too powerful and the 140 μJ IR condition may have achieved enough metal-silicon mixing for contact formation. The 140 μJ IR

condition may have already over-fired the sample and exposed more silicon than necessary. Future experiments should perform a parameter sweep that includes weaker IR energy doses.

To summarize, Si:Al ratios can provide valuable information about contact formation. The data for Group 1, 2, and 3 indicate that Si:Al may correlate with the amount of silicon exposed and LFC formation. For the tested conditions, it is unclear whether a simultaneous “Green + IR” lasing condition is superior to a single laser condition, although it seems that the green and IR lasers individually may perform as described in 4.1.

From the “IR only” lasing conditions, the PL contrast, SEM micrographs, and Si:Al ratios suggest that the microsecond time scales allow silicon to alloy with aluminum and form a contact. With the nanosecond green pulses, the Si:Al ratio needs further interpretation because silicon counts can be high due to repeated ablation at the surface, without alloying. A larger parameter search that includes lower energy doses may yield a simultaneous firing sequence that results in a lower R_C than for the same green or IR laser by itself, but a conclusion cannot be made from the data presented here.

4.3 XRF vs. EDS

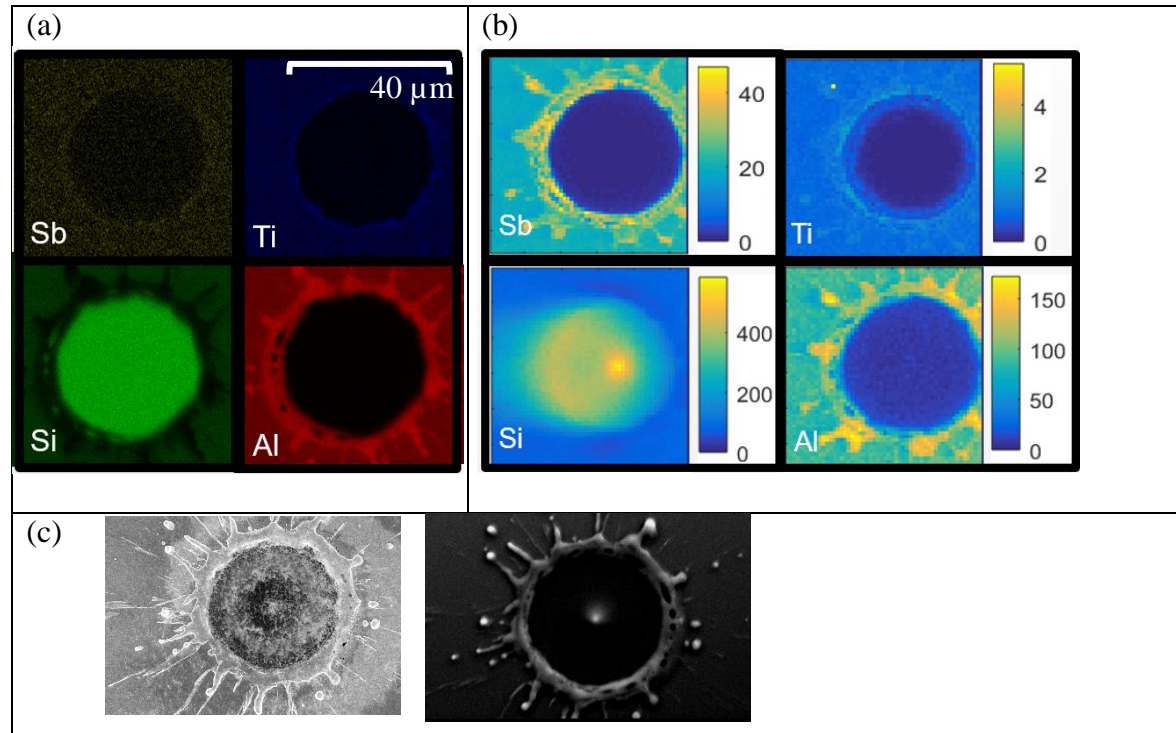


Figure 14 (a) EDS maps, (b) μ -XRF maps, and (c) two SEM images of the same “IR 2” spot, which highlight different features. The scale bar shown applies to all maps. The same μ -XRF maps were shown in Table 4 (35), but in \log_{10} scale. Here, the maps are linear.

A qualitative comparison between the two elemental mapping methods suggests that the sensitivity of μ -XRF is superior to that of EDS. In the silicon channel, the EDS map shows the splatter perimeter, the boundary between the silicon-rich hole and the surrounding ring, and some spots along the ring. Blurring in the μ -XRF silicon channel results in the same features not being sharply resolved, but a region of high silicon counts is visible only in the LFC center in the μ -XRF map. The high silicon region is corroborated by a peak in the center of the SEM image. The EDS map likely does not show it because the high silicon counts saturated the EDS detector, resulting in a map that appears relatively homogenous in the LFC center.

The metal channels show additional features and interfaces that are not resolvable by EDS. In the aluminum, antimony, and titanium channels, μ -XRF reveals two count levels within the center metal-poor hole. This differentiation in elemental counts indicates the extent to which molten material was expelled from the center, before resolidifying. The high antimony and titanium metal counts in the splatter rings in the μ -XRF channels, but not in EDS, indicate that significant amounts of those elements end up outside the contact-forming region. Since the antimony is intended to dope the exposed silicon, this additional information presents opportunities for process optimization.

The difference between the EDS and μ -XRF maps can be understood by the detection limits of each technique. The detection limit of EDS is approximately .001 ppm (by mass), whereas the μ -XRF detection limit is approximately .000001 ppm (by mass). As seen in Table 1, the atomic area density for titanium, antimony and aluminum are calculated using the atomic density and the thickness of each material layer. In the aluminum channel, EDS has sufficient sensitivity to distinguish between the metal-rich splatter and background. The areal density of antimony is 10x less than aluminum, and 100x less for antimony. μ -XRF provides three orders of magnitude more sensitivity than EDS. This presents new opportunities for LFC characterization and laser process optimization.

	Titanium	Aluminum	Antimony
Atoms per cm²	2.79E+16	3.01E+18	1.65E+17

Table 13 The approximate areal density of elements in the samples studied.

5. Summary & Conclusion

Decreasing the cost of PV manufacturing can encourage global adoption of solar power. Silicon remains the dominant solar cell material. Cell efficiency is affected by minority carrier lifetime. New architectures promise high industrial efficiencies, but require new manufacturing techniques. The implementation of LFCs can allow architectures like PERC to reach commercialization, but laser processing silicon with minimal damage remains a challenge. I hypothesize that a simultaneous two-laser firing process can achieve the same LFC R_C with less lifetime damage than the standard single-laser firing process, and that synchrotron μ -XRF capabilities can provide a novel way to characterize LFC quality.

In this thesis, I used structural characterization, including μ -XRF and SEM, and electrical characterization (TLM and PC-PLI), to compare contact quality and process-induced degradation in LFCs after single- and double-laser firing. I found that within this parameter set, a single IR laser process is sufficient for contact formation, but a single green laser does not form contact. Adding green lasers for simultaneous “Green + IR” firing does not seem to improve R_C or reduce minority carrier lifetime degradation. Minority carrier lifetime degradation does seem to rely on the energy dose of the IR laser, as longer and more energetic pulses result in a larger laser-damaged. Further tests should be done at lower energy doses to determine whether simultaneous firing can be effective.

The structural characterization demonstrated that Si:Al ratio from μ -XRF can be used to determine whether contact has been formed or not. The elemental sensitivity and resolution of μ -XRF lends insight into LFC formation immediately after lasing and the different elemental compositions across the region of interest. The SEM images indicated that the Green laser addition created craters and did not improve contact.

X-ray fluorescence mapping techniques were also compared. In a map from the same LFC, μ -XRF resolves features and interfaces that are not resolvable by EDS. In the antimony channel, μ -XRF revealed that significant amounts of metal was expelled outside of the contact-forming region. Since antimony is a dopant, this additional information presents opportunities to design a gentler process that reflow the metal to the contact. The high sensitivity of μ -XRF also allowed for a sensitive measure of the Si:Al ratio in the contact, which can be used to indicate contact formation.

This research illuminates the need to better understand the structure-property-process relationship in LFCs. Efforts to optimize the material stack and lasing process require a suite of characterization that can provide high elemental sensitivity, structural information, and electrical characterization. μ -XRF can provide such sensitivity, and in this work, it was paired with other techniques to correlate LFC features with stages of contact formation.

In summary, the research presented in this thesis provides quantitative information about LFC contact formation, lifetime degradation, and elemental composition. From this information, next steps should include testing simultaneous firing with lower-energy lasing parameters. Other μ -XRF studies of LFCs could also be done to investigate a phenomenological relationship between the Si:Al ratio and R_C . These steps can contribute to the industrial implementation of high-lifetime, low-resistance localized contacts for high-efficiency silicon modules.

BIBLIOGRAPHY

- [1] N. P. Gillett, V. K. Arora, K. Zickfeld, S. J. Marshall, and W. J. Merryfield, “Ongoing climate change following a complete cessation of carbon dioxide emissions,” *Nat. Geosci.*, vol. 4, no. 2, pp. 83–87, 2011.
- [2] A. A. Agrawal, A. P. Hastings, M. T. J. Johnson, J. L. Maron, and J. Salminen, “Future CO₂ Emissions and Climate Change from Existing Energy Infrastructure,” *Science* (80.), vol. 5317, no. 2005, 2010.
- [3] U S Energy Information Administration, “Emissions of Greenhouse Gases in the United States 2009,” no. March, 2011.
- [4] D. M. Powell, M. T. Winkler, H. J. Choi, C. B. Simmons, D. B. Needleman, and T. Buonassisi, “Crystalline silicon photovoltaics: a cost analysis framework for determining technology pathways to reach baseload electricity costs,” *Energy Environ. Sci.*, vol. 5, no. 3, p. 5874, 2012.
- [5] S. Kurtz, H. Atwater, A. Rockett, T. Buonassisi, C. Honsberg, and J. Benner, “Solar research not finished,” *Nat. Photonics*, vol. 10, no. 3, pp. 141–142, 2016.
- [6] I. Fraunhofer Institute for Solar Energy Systems, “Photovoltaics report,” no. March, 2016.
- [7] C. Becker, D. Amkreutz, T. Sontheimer, V. Preidel, D. Lockau, J. Haschke, L. Jogsches, C. Klimm, J. J. Merkel, P. Plocica, S. Steffens, and B. Rech, “Polycrystalline silicon thin-film solar cells: Status and perspectives,” *Sol. Energy Mater. Sol. Cells*, vol. 119, pp. 112–123, 2013.
- [8] S. Riegel, F. Mutter, T. Lauermann, B. Terheiden, and G. Hahn, “Review on screen printed metallization on p-type silicon,” *Energy Procedia*, vol. 21, no. October 2011, pp. 14–23, 2011.
- [9] S. Schramm, R. Trassl, A. M. GmbH, and C. Kg, “BOUNDARY CONDITIONS FOR THE INDUSTRIAL PRODUCTION OF LFC CELLS RESULTS FROM THE JOINT PROJECT INKA Fraunhofer Institute for Solar Energy Systems (ISE), Heidenhofstrasse 2 , D-79110 Freiburg , Germany ² Deutsche Cell GmbH , Berthelsdorfer Strasse 111A , ,”

pp. 3–6, 2006.

- [10] S. W. Glunz, R. Preu, and D. Biro, *Crystalline Silicon Solar Cells*, vol. 1. 2012.
- [11] “No Title.” [Online]. Available:
http://www.elp.uji.es/juan_home/images/solar_cell/princip.jpg.
- [12] J. Schmidt, B. Lim, D. Walter, K. Bothe, S. Gatz, T. Dullweber, and P. P. Altermatt, “Impurity-related limitations of next-generation industrial silicon solar cells,” *IEEE J. Photovoltaics*, vol. 3, no. 1, pp. 114–118, 2013.
- [13] D. J. Fitzgerald and A. S. Grove, “Surface Recombination in Semiconductors,” 1966.
- [14] A. M. Smith and S. Nie, “NIH Public Access,” vol. 43, no. 2, pp. 190–200, 2010.
- [15] A. G. Aberle, “Surface passivation of crystalline silicon solar cells: a review,” *Prog. Photovoltaics Res. Appl.*, vol. 8, no. 5, pp. 473–487, 2000.
- [16] W. Moench, *Semiconductor Surfaces and Interfaces*. .
- [17] H. Angermann, W. Henrion, M. Rebien, and A. Röseler, “Wet-chemical passivation and characterization of silicon interfaces for solar cell applications,” *Sol. Energy Mater. Sol. Cells*, vol. 83, no. 4, pp. 331–346, 2004.
- [18] J. M. . Langer and W. Walukiewicz, “Surface Recombination in Semiconductors,” *Surf. Sci.*, vol. 9, no. 2, p. 347–&, 1995.
- [19] W. Kern, “The evolution of silicon wafer cleaning technology,” *J. Electrochem. Soc.*, vol. 137, no. 6, pp. 1887–1892, 1990.
- [20] V. A. Burrows, Y. J. Chabal, G. S. Higashi, K. Raghavachari, and S. B. Christman, “Infrared spectroscopy of Si(111) surfaces after HF treatment: Hydrogen termination and surface morphology,” *Appl. Phys. Lett.*, vol. 53, no. 11, pp. 998–1000, 1988.
- [21] S. Rauscher, T. Dittrich, M. Aggour, J. Rappich, H. Flietner, and H. J. Lewerenz, “Reduced interface state density after photocurrent oscillations and electrochemical hydrogenation of n-Si(111): a surface photovoltage investigation,” *Appl. Phys. Lett.*, vol. 66, no. 111, pp. 3018–3020, 1995.

- [22] H. J. Lewerenz, K. Skorupska, M. Aggour, T. Stempel, and J. Grzanna, “Surface chemistry and electronics of semiconductor-nanosystem junctions I: Metal-nanoemitter-based solar cells,” *J. Solid State Electrochem.*, vol. 13, no. 2, pp. 185–194, 2009.
- [23] L. Zhao, C. Zhou, H. Li, H. Diao, and W. Wang, “Characterization on the Passivation Stability of HF Aqueous Solution Treated Silicon Surfaces for HIT Solar Cell Application by the Effective Minority Carrier Lifetime Measurement,” *Chinese J. Phys.*, vol. 48, no. 3, pp. 392–399, 2010.
- [24] J. J. Loferski, “Theoretical considerations governing the choice of the optimum semiconductor for photovoltaic solar energy conversion,” *J. Appl. Phys.*, vol. 27, no. 7, pp. 777–784, 1956.
- [25] W. Shockley, “The Theory of pn Junctions in Semiconductors and pn Junction Transistors,” *Bell Syst. Tech. J.*, vol. 28, no. 3, pp. 435–489, 1949.
- [26] M. A. Green and J. Nelson, *The physics of solar cells. Vol. 1*. London: Imperial College Press, 2003.
- [27] S. Basu, *Crystalline Silicon*, Second Edi. Elsevier Ltd, 2011.
- [28] A. Goodrich, P. Hacke, Q. Wang, B. Sopori, R. Margolis, T. L. James, and M. Woodhouse, “A wafer-based monocrystalline silicon photovoltaics road map: Utilizing known technology improvement opportunities for further reductions in manufacturing costs,” *Sol. Energy Mater. Sol. Cells*, vol. 114, pp. 110–135, Jul. 2013.
- [29] S. W. Glunz, a. Grohe, M. Hermle, E. Schneiderlochner, J. Dicker, R. Preu, H. Mackel, D. Macdonald, and a. Cuevas, “Analysis of laser-fired local back surface fields using n^{+/np^{+/}} cell structures,” *3rd World Conf. on Photovoltaic Energy Conversion, 2003. Proc.*, vol. 2, pp. 1332–1335, 2003.
- [30] E. Schneiderlochner, a Grohe, S. W. Glunz, R. Preu, and W. Willeke, “Processing in Silicon Solar Cell Manufacturing,” *Energy Convers.*, pp. 1364–1367, 2003.
- [31] I. S. Ramon Alcubilla, Carlos Molpeceres , Mónica Colina, David Muñoz-Martin, Isidro Martín, Pablo Ortega, “New Laser-based approaches to improve the passivation and rear contact quality in high efficiency crystalline silicon solar cells,” *SPIE 8826, Laser Mater.*

Process. Sol. Energy Devices II, vol. 8826, pp. 1–11, 2013.

- [32] M. Colina, I. Martín, C. Voz, A. Morales-Vilches, P. Ortega, G. López, A. Orpella, M. García-Molina, D. Muñoz-Martín, M. I. Sánchez-Aniorte, C. Molpeceres, and R. Alcubilla, “Optimization of Laser Processes for Local Rear Contacting of Passivated Silicon Solar Cells,” *Energy Procedia*, vol. 44, no. May 2013, pp. 234–243, 2014.
- [33] D. Spiers, *Practical Handbook of Photovoltaics*. Elsevier, 2012.
- [34] C. Haase, “More of Everything: Market survey on solar modules,” *Photon International*, 2011.
- [35] T. Saga, “Advances in crystalline silicon solar cell technology for industrial mass production,” *NPG Asia Mater.*, vol. 2, no. 3, pp. 96–102, 2010.
- [36] C. M. Dunsky, “<title>The promise of solar energy: applications and opportunities for laser processing in the manufacturing of solar cells</title>,” vol. 6459, p. 64590M–64590M–12, Feb. 2007.
- [37] J. Gifford, “Multicrystalline PERC to deliver 25% efficiencies,” *PV Magazine*, 2015.
- [38] A. Goodrich, T. James, and M. Woodhouse, “Utility-Scale Photovoltaic (PV) System Prices in the United States : Current Drivers and Cost-Reduction Opportunities Residential , Commercial , and Utility-Scale Photovoltaic (PV) System Prices in the United States : Current Drivers and Cost-Reductio,” no. February, 2012.
- [39] D. M. Powell, M. T. Winkler, A. Goodrich, and T. Buonassisi, “Modeling the cost and minimum sustainable price of crystalline silicon photovoltaic manufacturing in the united states,” *IEEE J. Photovoltaics*, vol. 3, no. 2, pp. 662–668, 2013.
- [40] D.-H. Neuhaus and A. Münzer, “Industrial Silicon Wafer Solar Cells,” *Adv. Optoelectron.*, vol. 2007, pp. 1–15, 2007.
- [41] W. Sidhu, Rubin; Bennett, Murray; Hmung, George; Ren, “Interdigitated back contact silicon solar cells with laser fired contacts,” *IEEE 39th Photovolt. Specialists Conf.*, pp. 1298–1300, 2013.
- [42] I. Zanesco, A. Moehlecke, J. L. Pinto, and M. Ly, “Development and Comparison of

Small and Large Area Boron Doped Solar Cells in n-type and p-type Cz-Si,” pp. 2284–2288, 2011.

- [43] M. Tucci, E. Talgorn, L. Serenelli, E. Salza, M. Izzi, and P. Mangiapane, “Laser fired back contact for silicon solar cells,” *Thin Solid Films*, vol. 516, no. 20, pp. 6767–6770, 2008.
- [44] E. Schneiderl~~och~~chner, R. Preu, R. L~~ed~~emann, and S. W. Glunz, “Laser-fired rear contacts for crystalline silicon solar cells,” *Prog. Photovoltaics Res. Appl.*, vol. 10, no. 1, pp. 29–34, Jan. 2002.
- [45] S. W. Glunz, E. Schneiderlöchner, D. Kray, A. Grohe, M. Hermle, H. Kampwerth, R. Preu, and G. Willeke, “LASER - FIRED CONTACT SILICON SOLAR CELLS ON p - AND n - SUBSTRATES.”
- [46] A. Grohe, E. Schneiderlochner, M. Hermle, and R. Preu, “Characterization of Laser-fired contacts processed on wafers with different resistivity,” pp. 18–21, 2003.
- [47] D. Kray and S. Glunz, “Investigation of laser-fired rear-side recombination properties using an analytical model,” *Prog. Photovoltaics Res. Appl.*, 2006.
- [48] J. Tous, Loic; Russel, Richard; Aleman, Monica; Duerinckx, Filip; Labie, Riet; Bertens, Jurgen; Horiuchi, Takeshi; Szlufcik, “Cost-effective and reliable Ni/Cu plating for p- and n-type PERx silicon solar cells yielding efficiencies above 20,5%,” *Photovoltaics Int.*, vol. 21, 2013.
- [49] J. Benick, B. Hoex, M. C. M. Van De Sanden, W. M. M. Kessels, O. Schultz, and S. W. Glunz, “High efficiency n-type Si solar cells on Al₂O₃-passivated boron emitters,” *Appl. Phys. Lett.*, vol. 92, no. 25, p. 253504, 2008.
- [50] S. W. Glunz, E. Schneiderlöchner, D. Kray, A. Grohe, M. Hermle, H. Kampwerth, R. Preu, and G. Willeke, “LASER-FIRED CONTACT SILICON SOLAR CELLS ON p- AND n-SUBSTRATES,” no. June, pp. 3–6, 2004.
- [51] E. Schneiderl~~och~~chner, R. Preu, R. L~~ed~~emann, and S. W. Glunz, “Laser-fired rear contacts for crystalline silicon solar cells,” *Prog. Photovoltaics Res. Appl.*, 2002.

- [52] A. A. Istratov, H. Hieslmair, and E. R. Weber, “Iron contamination in silicon technology,” *Appl. Phys. A Mater. Sci. Process.*, vol. 70, no. 5, pp. 489–534, 2000.
- [53] H. Booth, “Laser Processing in Industrial Solar Module Manufacturing,” *J. Laser Micro/Nanoengineering*, vol. 5, no. 3, pp. 183–191, Dec. 2010.
- [54] O. Haupt, V. Schütz, and U. Stute, “Multi-Spot Laser Processing of Crystalline Solar Cells,” *SPIE*, vol. 7921, p. 79210V–79210V–9, 2011.
- [55] C. Molpeceres, M. I. Sánchez-Aniorte, M. Morales, D. Muñoz, I. Martín, P. Ortega, M. Colina, C. Voz, and R. Alcubilla, “Influence of wavelength on laser doping and laser-fired contact processes for c-Si solar cells,” vol. 8473, p. 847308, 2012.
- [56] M. Ametowobla, J. R. Köhler, A. Esturo-Bretón, and J. H. Werner, “Improved Laser Doping for Silicon Solar Cells,” *22nd Eur. Photovolt. Sol. Energy Conf. Exhib.*, no. February, p. 1403, 2007.
- [57] M. Kim, D. Kim, D. Kim, and Y. Kang, “Analysis of laser-induced damage during laser ablation process using picosecond pulse width laser to fabricate highly efficient PERC cells,” *Sol. Energy*, vol. 108, pp. 101–106, 2014.
- [58] L. Bounaas, N. Auriac, B. Grange, R. Monna, M. Pirot, S. De Vecchi, J. Jourdan, S. Mialon, M. Pasquinelli, and D. Barakel, “Laser Ablation of Dielectric Layers and Formation of Local Al-BSF in Dielectric back Passivated Solar Cells,” *Energy Procedia*, vol. 38, pp. 670–676, Jan. 2013.
- [59] B. L. Decesar, “By,” no. May, 2010.
- [60] I. Sánchez-Aniorte, R. Barrio, a. Casado, M. Morales, J. Cárate, J. J. Gandía, and C. Molpeceres, “Optimization of laser-firing processes for silicon-heterojunction solar-cell back contacts,” *Appl. Surf. Sci.*, vol. 258, no. 23, pp. 9443–9446, 2012.
- [61] A. B. . Morales-Vilches, C. . Voz, M. . Colina, D. . Munoz-Martin, I. . Martin, P. R. . Ortega, G. . Lopez-Rodriguez, C. . Molpeceres, and R. . Alcubilla, “Study of the Surface Recombination Velocity for Ultraviolet and Visible Laser-Fired Contacts Applied to Silicon Heterojunction Solar Cells,” *IEEE J. Photovoltaics*, vol. 5, no. 4, pp. 1006–1013, 2015.

- [62] B. L. Decesar, “INVESTIGATION OF PROCESS PARAMETER OPTIMIZATION OF LASER-FIRED BACK CONTACT SILICON SOLAR CELLS,” *MS Thesis*, *Pennsylvania State Univ.*, no. May, 2010.
- [63] D. Suwito, U. Jäger, J. Benick, S. Janz, M. Hermle, R. Preu, and S. W. Glunz, “INdustrially feasible Rear Side Concept for n-type Silicon SOlar Cells Approaching 700 mV of VOC,” *25th Eur. Photovolt. Sol. Energy Conf.*, no. September, pp. 1443–1445, 2010.
- [64] F. Colville, “UV lasers in solar cell manufacturing: Enabling increased cell efficiency & yield,” 2009.
- [65] A. Raghavan, T. A. Palmer, and T. Debroy, “Evolution of laser-fired aluminum-silicon contact geometry in photovoltaic devices,” *J. Appl. Phys.*, vol. 111, no. 2, pp. 0–9, 2012.
- [66] J. Nekarda, M. Graf, A. Rodofili, A. Wolf, and R. Preu, “Laser-based foil rear side metallization for crystalline silicon solar cells,” *Proc. SPIE*, vol. 8473, p. 847307, 2012.
- [67] J. M??ller, K. Bothe, S. Gatz, H. Plagwitz, G. Schubert, and R. Brendel, “Recombination at local aluminum-alloyed silicon solar cell base contacts by dynamic infrared lifetime mapping,” *Energy Procedia*, vol. 8, pp. 337–342, 2011.
- [68] X. He, T. Debroy, and P. W. Fuerschbach, “Alloying element vaporization during laser spot welding of stainless steel,” *J. Phys. D Appl. Phys. J. Phys. D Appl. Phys.*, vol. 36, no. 36, pp. 3079–3088, 2003.
- [69] T. A. P. Ashwin S. Raghavan, “Employing microsecond pulses to form laser-fired contacts in photovoltaic devices,” *Prog. Photovolt Res. Appl.*, vol. 23, no. June 2014, pp. 1025–1036, 2015.
- [70] a. Raghavan, T. a. Palmer, a. Domask, S. Mohney, E. W. Reutzel, and T. DebRoy, “Role of processing parameters on morphology, resistance and composition of laser fired contacts,” vol. 8826, p. 882606, 2013.
- [71] P. Kumar, K. Wijekoon, M. Agrawal, K. Rapolu, H. Munegkar, M. Stewart, J. Franklin, Y. Zheng, F. Yan, A. Chan, X. Lu, D. Kochhar, M. Vellaikal, L. Zhang, V. Dabeer, D. Tanner, and H. Ponnekanti, “Progress in production-worthy point contact solar cells

- process,” *Conf. Rec. IEEE Photovolt. Spec. Conf.*, pp. 2186–2191, 2012.
- [72] I. Martin, M. Labrune, a. Salomon, P. Roca I Cabarrocas, and R. Alcubilla, “Laser fired contacts applied to the rear surface of heterojunction silicon solar cells,” *Sol. Energy Mater. Sol. Cells*, vol. 95, no. 11, pp. 3119–3123, 2011.
- [73] M. Colina, A. B. Morales-Vilches, C. Voz, I. Mart??n, P. R. Ortega, and R. Alcubilla, “Low Surface Recombination in Silicon-Heterojunction Solar Cells With Rear Laser-Fired Contacts from Aluminum Foils,” *IEEE J. Photovoltaics*, vol. 5, no. 3, pp. 805–811, 2015.
- [74] C. H. Crouch, J. E. Carey, J. M. Warrender, M. J. Aziz, E. Mazur, and F. Y. Génin, “Comparison of structure and properties of femtosecond and nanosecond laser-structured silicon,” *Appl. Phys. Lett.*, vol. 84, no. 11, pp. 1850–1852, 2004.
- [75] A. Roig??, J. Alvarez, J. P. Kleider, I. Mart??n, R. Alcubilla, and L. F. Vega, “Microscale spatially resolved characterization of highly doped regions in laser-fired contacts for high-efficiency crystalline Si solar cells,” *IEEE J. Photovoltaics*, vol. 5, no. 2, pp. 545–551, 2015.
- [76] B. Fischer, “Loss analysis of crystalline silicon solar cells using photoconductance and quantum efficiency measurements,” *Naturwissenschaften*, p. 198, 2003.
- [77] S. Urabe, J. Irikawa, M. Konagai, and S. Miyajima, “Characterization of laser transferred contact through aluminum oxide passivation layer,” *Jpn. J. Appl. Phys.*, vol. 54, no. 8S1, p. 08KD02, 2015.
- [78] S. W. G. F. Granek, C. Reichel, M. Hermle, D. M. Huljic, O. Schultz, “Front surface passivation of n-type high-efficiency back-junction silicon solar cells using front surface field,” no. September, pp. 3–7, 2007.
- [79] E. Schneiderlochner, “Thesis,” University of Freiburg, 2004.
- [80] a. Raghavan, T. a. Palmer, and T. DebRoy, “Passivation layer breakdown during laser-fired contact formation for photovoltaic devices,” *Appl. Phys. Lett.*, vol. 105, no. 2, p. 024105, Jul. 2014.

- [81] I. Sánchez-Aniorte, M. Colina, F. Perales, and C. Molpeceres, “Optimization of laser fired contact processes in c-Si solar cells,” *Phys. Procedia*, vol. 5, pp. 285–292, 2010.
- [82] J. He, S. Hegedus, U. Das, Z. Shu, M. Bennett, L. Zhang, and R. Birkmire, “Laser-fired contact for n-type crystalline Si solar cells,” *Prog. Photovoltaics Res. Appl.*, no. 23, pp. 1091–1099, 2014.
- [83] R. a. Sinton and D. Macdonald, “WCT-120 Photoconductance Lifetime Tester and optional Suns-Voc Stage: User Manual.” Sinton Consulting, Inc., Boulder, CO.
- [84] T. Trupke and R. a. Bardos, “Photoluminescence: a surprisingly sensitive lifetime technique,” *Conf. Rec. Thirty-first IEEE Photovolt. Spec. Conf. 2005.*, pp. 903–906, 2005.
- [85] S. Herlufsen, J. Schmidt, D. Hinken, K. Bothe, and R. Brendel, “Photoconductance-calibrated photoluminescence lifetime imaging of crystalline silicon,” *Phys. status solidi - Rapid Res. Lett.*, vol. 2, no. 6, pp. 245–247, Dec. 2008.
- [86] T. Trupke, R. a. Bardos, M. C. Schubert, and W. Warta, “Photoluminescence imaging of silicon wafers,” *Appl. Phys. Lett.*, vol. 89, no. 4, p. 044107, 2006.
- [87] K. L. Luke and L. J. Cheng, “Analysis of the interaction of a laser pulse with a silicon wafer: Determination of bulk lifetime and surface recombination velocity,” *J. Appl. Phys.*, vol. 61, no. 6, pp. 2282–2293, 1987.
- [88] G. K. Reeves and H. B. Harrison, “Obtaining the specific contact resistance from transmission line model measurements,” *IEEE Electron Device Lett.*, vol. 3, no. 5, pp. 111–113, 1982.
- [89] R. Van Grieken and A. Markowicz, *Handbook of X-ray Spectrometry*. CRC Press, 2001.
- [90] M. Siegbahn, “X-ray Spectroscopy,” in *Fifty Years of X-Ray Diffraction*, E. E. Ewald, Ed. Springer US, 1962, pp. 265–276.
- [91] N. Available and O. X. D. Booklet, *X-ray data booklet*, vol. 8, no. 4. 2001.
- [92] M. West, A. T. Ellis, P. J. Potts, C. Strelí, C. Vanhoof, and P. Wobrauschek, “2014 Atomic Spectrometry Update – a review of advances in X-ray fluorescence spectrometry,” *J. Anal. At. Spectrom.*, vol. 29, no. 9, pp. 1516–1563, 2014.

- [93] S. Vogt, “No Title,” *Beamlines and Facilities: Beamline: 2-ID-D*, 2007. [Online]. Available:
http://www.aps.anl.gov/Xray_Science_Division/Xray_Microscopy_and_Imaging/Beamlines/2_ID_D/. [Accessed: 06-Oct-2016].
- [94] D. Fenning, “High-Temperature Defect Engineering for Silicon Solar Cells: Predictive Process Simulation and Synchrotron-Based Microcharacterization,” Massachusetts Institute of Technology, 2013.
- [95] A. E. Morishige, H. S. (Aalto U. Laine, M. A. (MIT) Jensen, P. X. T. (MIT) Yen, E. E. (MIT) Looney, S. (Argonne N. L. Vogt, B. (Argonne N. L. Lai, H. (Aalso U. Savin, and T. Buonassisi, “Accelerating Synchrotron-Based Characterization of Solar Materials: Development of Flyscan Capability,” *Photovolt. Spec. Conf.*, 2016.
- [96] S. P. Phang, H. C. Sio, and D. Macdonald, “Carrier de-smearing of photoluminescence images on silicon wafers using the continuity equation,” vol. 192112, pp. 101–104, 2013.
- [97] P. Ortega, A. Orpella, I. Mart??n, M. Colina, G. L??pez, C. Voz, M. I. S??nchez, C. Molpeceres, and R. Alcubilla, “Laser-fired contact optimization in c-Si solar cells,” *Prog. Photovoltaics Res. Appl.*, vol. 20, no. 2, pp. 173–180, 2012.
- [98] a Letsch, D. Bartl, M. Diez, R. Gauch, a Michalowski, and M. Hafner, “Laser processes for future solar cells,” *Proc. SPIE - Int. Soc. Opt. Eng.*, vol. 8243, p. 824317 (16 pp.), 2012.
- [99] M. S. Brown and C. B. Arnold, “Laser Precision Microfabrication,” vol. 135, pp. 91–120, 2010.
- [100] A. Clauer, J. Holbrook, and B. Fairand, “Effects of laser induced shock waves on metals,” *Shock Waves High-Strain-Rate Phenom. Met.*, no. 6, pp. 675–702, 1981.